

Magnetic reconnection plasmoid model for Sagittarius A* flares

N. Aimar¹, A. Dmytriiev², F. H. Vincent¹, I. El Mellah³, T. Paumard¹, G. Perrin¹, and A. Zech⁴

¹ LESIA, Observatoire de Paris, Université PSL, CNRS, Sorbonne Université, Université Paris Cité, 5 place Jules Janssen, 92195 Meudon, France

e-mail: nicolas.aimar@obspm.fr

² Centre for Space Research, North-West University, Potchefstroom, 2531, South Africa

³ Univ. Grenoble Alpes, CNRS, IPAG, 38000 Grenoble, France

⁴ LUTH, Observatoire de Paris, CNRS, Université Paris Diderot, 5 place Jules Janssen, 92190 Meudon, France

Received September 09, 2022; accepted January 27, 2023

ABSTRACT

Context. Sagittarius A*, the supermassive black hole at the center of our galaxy, exhibits episodic near-infrared flares. The recent monitoring of three such events by the GRAVITY instrument has shown that some flares are associated with orbital motions in the close environment of the black hole. The GRAVITY data analysis points at super-Keplerian azimuthal velocity, while (sub-)Keplerian velocity is expected for the hot flow surrounding the black hole.

Aims. We develop a semi-analytic model of Sagittarius A* flares based on an ejected large plasmoid, inspired by recent particle-in-cell global simulations of black hole magnetospheres. We model the infrared astrometric and photometric signatures associated to this model.

Methods. We consider a spherical macroscopic hot plasma region, that we call a large plasmoid. This structure is ejected along a conical orbit in the vicinity of the black hole. This plasmoid is assumed to be formed by successive mergers of smaller plasmoids produced through magnetic reconnection that we do not model. Non-thermal electrons are injected in the plasmoid. We compute the evolution of the electron-distribution function under the influence of synchrotron cooling. We solve the radiative transfer problem associated to this scenario and transport the radiation along null geodesics of the Schwarzschild spacetime. We also take into account the quiescent radiation of the accretion flow, on top of which the flare evolves.

Results. For the first time, we successfully account for the astrometric and flux variations of the GRAVITY data with a flare model that incorporates an explicit modeling of the emission mechanism. We find good agreement between the prediction of our model and the recent data. In particular, the azimuthal velocity of the plasmoid is set by the magnetic field line it belongs to, which is anchored in the inner parts of the accretion flow, hence the super-Keplerian motion. The astrometric track is also shifted with respect to the center of mass due to the quiescent radiation, in agreement with the difference measured with the GRAVITY data.

Conclusions. These results support the picture of magnetic reconnection in a black hole magnetosphere as a viable model for Sagittarius A* infrared flares.

Key words. Accretion, accretion disk - Magnetic reconnection - Black hole physics - Relativistic processes - Radiative transfer - Radiation mechanisms: non-thermal

1. Introduction

The Galactic Center hosts the compact radio source Sagittarius A* (Sgr A*) with an estimated mass of 4.297 million solar masses at a distance of only 8.277 kpc (GRAVITY Collaboration et al. 2022). This makes the compact object associated to Sgr A* the closest supermassive black hole (SMBH) candidate to Earth. Sgr A* is a low-luminosity accretion flow with an accretion rate of $(5.2 - 9.5) \times 10^{-9} M_{\odot} \text{ yr}^{-1}$ and a bolometric luminosity of $(6.8 - 9.2) \times 10^{35} \text{ erg s}^{-1}$ (Bower et al. 2019; Event Horizon Telescope Collaboration et al. 2022b) and thus is accreting at a very sub-Eddington rate. It has been the subject of numerous observing campaigns over the past two decades in order to test the massive black hole (MBH) paradigm (see Gravity Collaboration et al. (2020b)) and study the physics of radiatively inefficient accretion flows (RIAF) around SMBH.

Sgr A* shows a slow and low amplitude variability in radio (Lo et al. 1975; Backer 1978; Krichbaum et al. 1998; Falcke 1999; Bower et al. 2006; Michail et al. 2021b), in millimetre and submillimetre (Mauerhan et al. 2005; Macquart et al. 2006;

Yusef-Zadeh et al. 2006; Marrone et al. 2008; Brinkerink et al. 2015; Wielgus et al. 2022a), but also large amplitude and rapid variability in near infrared (NIR; Genzel et al. 2003; Ghez et al. 2004; Hornstein et al. 2007; Hora et al. 2014) and in X-rays (Baganoff et al. 2001; Nowak et al. 2012; Neilsen et al. 2013; Barrière et al. 2014; Ponti et al. 2015). The flux distribution in the NIR of Sgr A* has been the subject of numerous studies. Some claim a single state modeled by rednoise (Witzel et al. 2018; Do et al. 2019) for the variability of Sgr A* while others claim that there are two states for Sgr A* (Genzel et al. 2003; Dodds-Eden et al. 2011; Gravity Collaboration et al. 2020a; Witzel et al. 2021): a continuously low amplitude variable state called "quiescent state" and the "flare state" described by short and bright flux with a typical timescale of 30 minutes to 1 hour with a rate of ~ 4 a day. Multi-wavelength studies show that when an X-ray flare is observed, there is a counterpart in NIR suggesting a common origin but the reverse is not true (Fazio et al. 2018). Moreover, the flare can also be observed in sub-mm but with a time lag of several minutes (Eckart et al. 2008, 2009; Dodds-Eden et al. 2009; Michail et al. 2021a; Witzel et al.

2021) following a dimming (Wielgus et al. 2022a; Ripperda et al. 2022).

Recently, the GRAVITY instrument (Gravity Collaboration et al. 2017; Eisenhauer et al. 2008, 2011; Paumard et al. 2008) was able to resolve the motion of the NIR centroid during three bright flare events, showing a clockwise, continuous rotation at low inclination close to face-on ($i \sim 20^\circ$) consistent with a region of emission located at a few gravitational radii $r_g = GM/c^2$ from the central black hole (Gravity Collaboration et al. 2018). These flares are thus powered very close to the event horizon of the black hole. The exploration of a relativistic accretion region as close to the event horizon with high-precision astrometry and imaging techniques like GRAVITY and the Event Horizon Telescope (EHT) (Event Horizon Telescope Collaboration et al. 2022a) promises important information for physics and astronomy, including new tests of the MBH paradigm.

Significant efforts have been made to explain the flares of Sgr A*: rednoise (Do et al. 2009), hot spot (Hamaus et al. 2009; Genzel et al. 2003; Broderick & Loeb 2006), ejected blob (Vincent et al. 2014), star-disk interaction (Nayakshin et al. 2004) and disk instability (Tagger & Melia 2006). The GRAVITY observations in 2018 (Gravity Collaboration et al. 2018) support the hot spot model. However, the physical origin of such hot spots remains an open question. Instabilities in black hole accretion disks are a candidate, for instance the triggering of Rossby Waves Instabilities (RWI; Tagger & Melia 2006; Vincent et al. 2014). Alternatively, it could originate from the dissipation of electromagnetic energy through magnetic reconnection. This modification of the magnetic field topology results from the inversion of the magnetic field orientation across a current sheet which eventually breaks into magnetic islands called plasmoids (Komissarov 2004, 2005; Komissarov & McKinney 2007; Loureiro et al. 2007; Sironi & Spitkovsky 2014; Parfrey et al. 2019; Ripperda et al. 2020; Porth et al. 2021). In the past years, numerical simulations have repeatedly highlighted the ubiquity of magnetic reconnection in BH magnetospheres, whatever the physical point of view adopted: global particle-in-cell (PIC) simulations in Kerr metrics (El Mellah et al. 2022; ?), resistive general-relativistic magneto-hydrodynamics (GRMHD) simulations (Ripperda et al. 2020; Dexter et al. 2020a,b) or resistive force-free simulations (Parfrey et al. 2015). PIC simulations show that magnetic reconnection in the collisionless corona of spinning BHs can accelerate leptons up to relativistic Lorentz factors of $\gamma \sim 10^{3...7}$ (El Mellah et al. 2022), sufficiently high to generate the variable IR (and X-ray) emission (Rowan et al. 2017; Werner et al. 2018; Ball et al. 2018; Zhang et al. 2021; Scepi et al. 2022).

The GRMHD and PIC frameworks each have different limitations. GRMHD simulations describe the evolution of the accretion flow over long time scales, typically of the order of several $100,000 r_g/c$, but they rely on a fluid representation. Consequently, they cannot self-consistently capture the kinetic effects which are important to constrain dissipation, particle acceleration and subsequent non-thermal radiation. On the other hand, PIC simulations provide an accurate description of the microphysics but at the cost of simulations which can only span a few $100 r_g/c$ in time and with limited scale separation between global scales and plasma scales.

We develop a semi-analytical model, fed by the knowledge accumulated by recent GRMHD and GRPIC simulations. The aim is to condense into a reasonably small set of simple parameters the complex physics of GRMHD and GRPIC models, and thus allow to probe a large parameter space within a reasonable computing time. We also want to remain as agnostic as possi-

ble regarding the initial conditions of the flow. In this context, we discuss the interpretation of the Gravity Collaboration et al. (2018) flare data paying particular attention to the following diagnostics:

- the marginally detected shift between the astrometric data and the center-of-mass location;
- the tension between the data and the hot spot model used by Gravity Collaboration et al. (2018), which assumes a Keplerian orbit;
- the physical origin of the rising and decaying phases of the flare light curve in the context of magnetic reconnection.

The first point can be discussed in the context of a very simple hot-spot model and is the main topic of Sect. 2. Sect. 3 is the core of our study and focuses on the second and third points above. It presents a semi-analytical large plasmoid model due to magnetic reconnection. It highlights in particular the impact of considering a self-consistent evolution of the electron distribution function through kinetic modeling. This section shows that our plasmoid model is able to reasonably account for the Gravity Collaboration et al. (2018) flare data. The limitations of our plasmoid model are discussed in Sect. 4. The conclusions and perspectives are given in Sect. 5.

2. Quiescent flow impact on astrometry: shifting and rotating the orbit

Gravity Collaboration et al. (2018) used a hot spot model in an equatorial circular orbit to fit the astrometry of three bright flares. They considered a constant radiation flux from the emitting region orbiting the black hole to fit the orbital motion. The effect of out-of-plane motion and orbital shear have also been studied by Gravity Collaboration et al. (2020c) to model the flares. However, the impact of the quiescent radiation surrounding the hot spot was not taken into account. The aim of this section is to show that taking into account the quiescent radiation can lead to shifting and rotating the orbit on sky. We note a $1-\sigma$ difference between the center of the orbit of the hot spot and the center of mass derived from the orbit of S2 in Gravity Collaboration et al. (2018) which makes this shift marginal.

In this section, we will use a simplified hot spot model that is sufficient to highlight the main effects of the quiescent radiation. This simple model will also allow us to introduce the most important relativistic effects at play, that were already studied in many previous works (Broderick & Loeb 2006; Hamaus et al. 2009). These reminders will be helpful when we turn to a more complex hot spot model in the Sect. 3, which is the main aim of this paper.

2.1. Simple hot spot + quiescent model for the flaring Sgr A*

The quiescent radiation of Sgr A* is modeled by means of the torus-jet model as derived in Vincent et al. (2019), to which we refer for all details. Figure 1 resumes the main features of the model. The torus emits thermal synchrotron radiation, while the flux emitted by the jet follows a κ distribution (i.e. a thermal core with a power-law tail). The multi-wavelength spectrum of the quiescent Sgr A* is well fit with this model. The κ distribution emission from the jets dominates at most wavelength except at the sub-mm bump where the flux comes mostly from the thermal disk. We summarize the best-fit parameters in Table 1, and the resulting best-fit quiescent spectrum is given in Fig. 2. More details on the fitting procedure are given in Appendix A. With

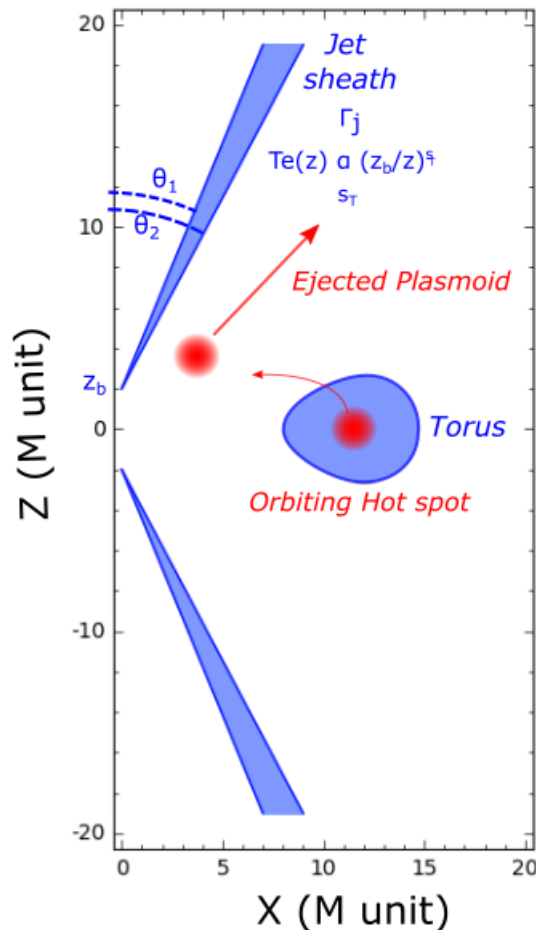


Fig. 1. Scheme of the torus-jet model for the quiescent state in blue and flares in red. Two trajectories are considered for the flare, which can either rotate in the torus (hot spot model) or be ejected along the jet sheath (plasmoid model). The jet is parametrized by the angles θ_1 and θ_2 that describe the angular opening of the radiation-emitting sheath, by the base height z_b , the constant Lorentz factor Γ_j , and the temperature power-law index s_T . The jet is symmetrical with respect to the equatorial plane, and axisymmetric.

these parameters, the flux of the torus-jet model at $2.2 \mu\text{m}$ is 1.1 mJy . It is in perfect agreement with the median quiescent dereddened flux provided by Gravity Collaboration et al. (2020a) of $1.1 \pm 0.3 \text{ mJy}$. At this wavelength, the torus is optically thin and its emission is negligible compared to the jet. In the remainder of this paper, where we focus only on the infrared band, we will thus neglect the torus and consider a pure jet quiescent model, unless otherwise noted.

The only relevant features of our quiescent model for the rest of this paper are the location of its infrared centroid and its NIR flux. As depicted in the right panel of Fig. 2, the centroid of our jet-dominated model lies very close to the mass center. We have checked that considering a disk-dominated model only very marginally changes the position of the quiescent centroid at low inclination (see the blue and green dots in the left panel of Fig. 3). Our conclusions are thus not biased by our particular choice of a jet-dominated quiescent model.

The hot spot model is composed of a plasma sphere of radius $1 r_g$ (fixed) with a uniform but time-dependent κ -distribution for the electrons. The emissivity j_ν and absorptivity α_ν coefficients depend on the density, temperature, and magnetic field which we considered uniform. We use the fitting formula of Pandya et al. (2016) to compute these coefficients. The typical light curve of a flare is characterized by a phase with increasing flux and one

with decreasing flux. We model this behavior by a Gaussian time modulation on the density and temperature as follows

$$n_e(t) = n_e^{hs} \exp\left(-0.5 \times \left(\frac{t - t_{ref}}{t_\sigma}\right)^2\right), \quad (1)$$

$$T_e(t) = T_e^{hs} \exp\left(-0.5 \times \left(\frac{t - t_{ref}}{t_\sigma}\right)^2\right) \quad (2)$$

where t_σ is the typical duration of the flare. As n_e varies over time (Eq. 1), the magnetic field strength also varies since we set a constant magnetization $\sigma = B^2/4\pi m_p c^2 n_e$.

Contrary to Gravity Collaboration et al. (2020c), we keep the circular equatorial orbit of Gravity Collaboration et al. (2018) as we assume that the hot spot is formed in the equatorial plane and we do not take into account any shearing effect and assume a constant spherical geometry of the hot spot. We summarize all the input parameters of the hot spot in Table 2.

2.2. Shifting the orbit on sky

Figure 3 shows the impact of taking into account the quiescent radiation on the astrometry of the flare, considering the trivial

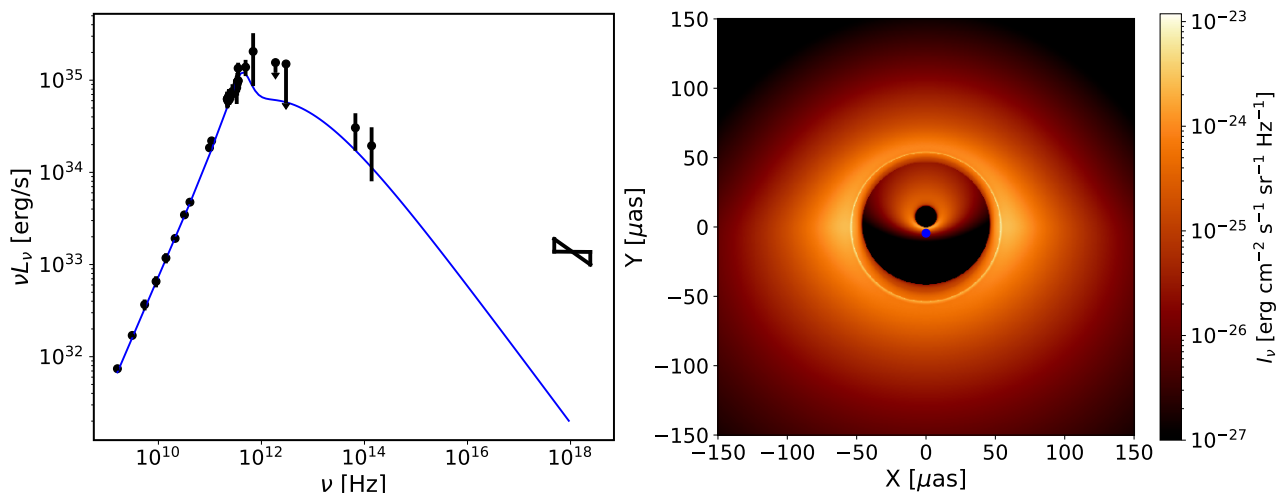


Fig. 2. **Left:** Spectrum associated to the best-fit of the torus-jet model (see Table 1) for the quiescent state of Sgr A* ($\chi^2_{red} = 0.91$ with $\text{ndof}=27$). The data are taken from Bower et al. (2015) for $\nu < 50$ GHz, Brinkerink et al. (2015) for the 2 points around 100 GHz, Liu et al. (2016) for the 492 GHz point, Marrone et al. (2006) for the 690 GHz point, von Fellenberg et al. (2018) for the far infrared upper limits, Witzel et al. (2018) for the mid infrared data, and Baganoff et al. (2001) for the X-ray bow-tie. We note that as in Vincent et al. (2019), the X-ray data are not fitted as we do not take into account bremsstrahlung nor Comptonized emission. **Right:** Best-fit image at $2.2 \mu\text{m}$ of the torus-jet model with a field of view of $150 \mu\text{as}$ seen with an inclination of 20° and a Position Angle of the Line of Nodes (PALN) of π rad. The color bar gives the values of specific intensity in cgs units in log-scale. The outer region emission comes from the backward jet’s part while the emission close to the center comes from the forward part of the jet. The centroid of the jet is represented by the blue dot at $\sim(0, -2.2)$.

Parameter	Symbol	Value
Black Hole		
mass [M_\odot]	M	4.297×10^6
distance [kpc]	d	8.277
spin	a	0
inclination [$^\circ$]	i	20
Torus		
angular momentum [r_g/c]	l	4
inner radius [r_g]	r_{in}	8
polytropic index	k	5/3
central density [cm^{-3}]	n_e^T	1.2×10^9
central temperature [K]	T_e^T	7×10^9
magnetization parameter	σ^T	0.002
Jet		
inner opening angle [$^\circ$]	θ_1	20
outer opening angle [$^\circ$]	θ_2	$\theta_1 + 3.5$
jet base height [r_g]	z_b	2
bulk Lorentz factor	Γ_j	1.15
base number density [cm^{-3}]	n_e^J	3.5×10^6
base temperature [K]	T_e^J	3×10^{10}
temperature slope	s_T	0.21
κ index	κ^J	5.5
magnetization parameter	σ^J	(fixed) 1

Table 1. Best fit parameters of the torus+jet quiescent model. We keep the same geometrical parameters, bulk Lorentz factor and κ -index as Vincent et al. (2019) and we fit the base number density, base temperature and temperature slope of the jet considering the correction (see below) and the new value of the jet magnetization parameter. The parameters of the torus are unchanged.

case of a constant-emission hot spot, as well as the varying-emission hot spot introduced in section 2.1.

Obviously, whether or not the hot spot intrinsic emission varies, the first effect of adding a quiescent radiation is to shrink the orbit’s size, because the overall centroid is moved towards

the quiescent radiation’s centroid, which always lies close to the mass center.

A slightly less obvious effect is that, when the hot spot emission varies in time, the orbit can shift in the plane of sky, and no longer be centered at the center-of-mass location. This is clearly apparent on the solid-red orbit of the left panel of Fig. 3. This is simply due to the time variation of the intensity ratio between the quiescent and the hot spot radiation. At early and late times, the hot spot has a weaker emission than the quiescent component, and the overall centroid coincides with the quiescent centroid. As the hot spot emission increases and dominates, the overall centroid will be driven towards it. Such a shift between the astrometric data and the center-of-mass position is visible at $1\text{-}\sigma$ significance in the Gravity Collaboration et al. (2018) data.

We note another non-trivial effect appearing in the varying-emission hot-spot orbit without any quiescent radiation (red-dotted orbit in Fig. 3). The orbit is not closing, due to the time delay between the primary and secondary images. Indeed, at the end of the simulation, the flux from the secondary image is intrinsically higher than the primary (the emission times of the primary and secondary are different), and is amplified by the beaming effect. When the centroid is computed, the secondary image has a larger impact at this time than before, resulting in a closer centroid position relative to the black hole. This astrometric impact of the secondary image was already discussed by Hamaus et al. (2009).

2.3. Rotating the orbit on sky

It is not an easy task to disentangle the intrinsic time variability of the hot spot from the variability due to the relativistic beaming effect. Figure 4 illustrates the impact on astrometry and light curve of playing with the relative influence between the intrinsic and beaming-related variability. Here, we simply change the initial azimuthal coordinate φ_0 of the hot spot along its orbit, in order to change the dephasing between the time of the maximum intrinsic emission ($t = t_{\text{ref}}$) which is fixed, and the time

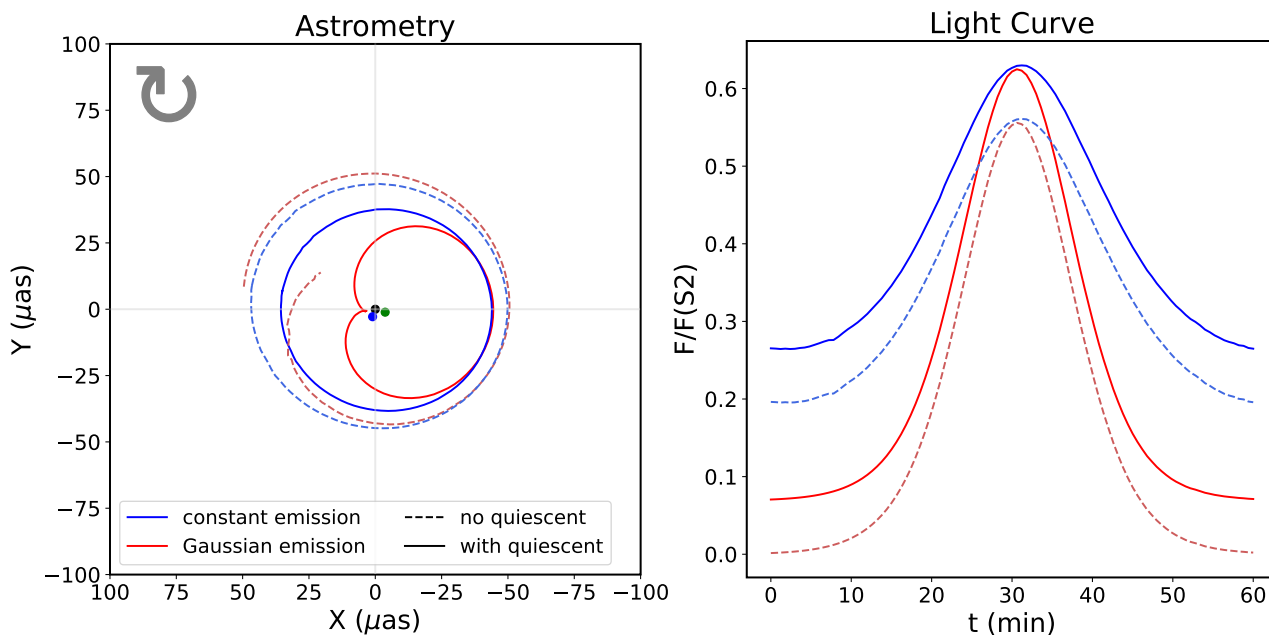


Fig. 3. Astrometry (left) and light curves (right) of the hot spot - jet model with two values for the quiescent state corresponding to *no quiescent* (dashed lines) and the *with quiescent state* (full lines). In shade of blue, the hot spot has a nearly constant emission ($t_\sigma \gg t_{orbit}$). The effect of beaming is reflected in the light curves. In shade of red, the hot spot has a Gaussian time emission with $t_\sigma = 30$ min. The parameters of the hot spot are listed in Table 2. We synchronise the maximum of Sgr A* of beaming and the intrinsic maximum of the Gaussian modulation. The black, blue and green dots in the left panels represent the position of Sgr A*, the jet’s centroid and the disk’s centroid respectively.

Parameter	Symbol	Value
Hot spot		
number density max [cm^{-3}]	n_e^{hs}	1.05×10^7
temperature max [K]	T_e^{hs}	9.03×10^{10}
time Gaussian sigma [min]	t_σ	30
magnetization parameter	σ^{hs}	0.01
κ -distribution index	κ^{hs}	5
orbital radius [r_g]	R^{hs}	9
initial azimuth angle [$^\circ$]	φ_0^{hs}	90
Position Angle of the Line of Nodes [$^\circ$]	Ω	160

Table 2. Summary of parameters of the hot spot model. We note that we used the maximum number density and temperature of the jet best-fit in Table 1 as reference and scale them for the hot spot by a factor 3.01.

of the maximum constructive beaming effect (when the hot spot moves towards the observer). The orbit rotates around the quiescent centroid following the variation of φ_0 (left panel of Fig. 4). The light curve is also strongly affected, reaching much brighter levels when the intrinsic emission maximum is in phase with the constructive beaming effect.

Here we show that the quiescent state of Sgr A* can have significant impact on the observed astrometry by shrinking the apparent orbit, creating a shift between the center of the latter and the position of the mass center. One should have these effects in mind for the comparison to the flare data at the end of the following section.

3. Plasmoid model from magnetic reconnection

In this section, we develop a semi-analytical hot-spot-like model in order to interpret the rise and decay of Sgr A* flares, thus going one step further with respect to the model we used in sec-

tion 2, where a Gaussian modulation of the emission is enforced without physical motivation.

Black hole magnetospheres naturally lead to the development of equatorial current sheets corresponding to a strong spatial gradient of the magnetic field which changes sign at the equator (Komissarov 2004; Komissarov & McKinney 2007; Parfrey et al. 2019; Ripperda et al. 2020). Such a configuration results in magnetic reconnection, i.e. a change of the topology of the field lines forming X points (Komissarov 2005; Loureiro et al. 2007; Sironi & Spitkovsky 2014). This process is intrinsically non-ideal and thus can only be captured either by resistive MHD or kinetic simulations. For suitable values of the magnetic diffusivity, the reconnecting current sheet can break into chains of plasmoids, i.e. magnetic islands separated by X points (Loureiro et al. 2007; Parfrey et al. 2019; Ripperda et al. 2020; Porth et al. 2021).

The reconnection rate (i.e. the typical rate at which magnetic energy is dissipated into particle kinetic energy) is equal to the ratio v_{rec}/v_{out} with v_{rec} the velocity of matter injected into the reconnection region, and v_{out} the bulk outflow velocity of particles accelerated by the reconnection event. The outflow velocity is of the order of the Alfvén speed, $v_{out} \approx v_A$, which is itself of the order of the speed of light, $v_A \approx c$, for strongly magnetized environments. The reconnection rate has been shown to be rather independent of the details of the chosen parameters. For PIC simulations, it lies around 10%, i.e. $v_{rec,PIC} \approx 0.1v_A \approx 0.1c$, for magnetized collisionless plasmas (Sironi & Spitkovsky 2014; Werner et al. 2018; Guo et al. 2015), which are the typical conditions in the inner flow surrounding Sgr A*¹. GRRMHD simulations point towards a slower rate of around 1%, so that $v_{rec,MHD} \approx 0.01c$ (see the discussion in Ripperda et al. 2022),

¹ It is likely that the accretion flow surrounding Sgr A* is in a Magnetically Arrested Disk (MAD, see Narayan et al. 2003) regime, i.e. with strong poloidal magnetic fields in the inner regions (Gravity Collaboration et al. 2018; Dexter et al. 2020b).

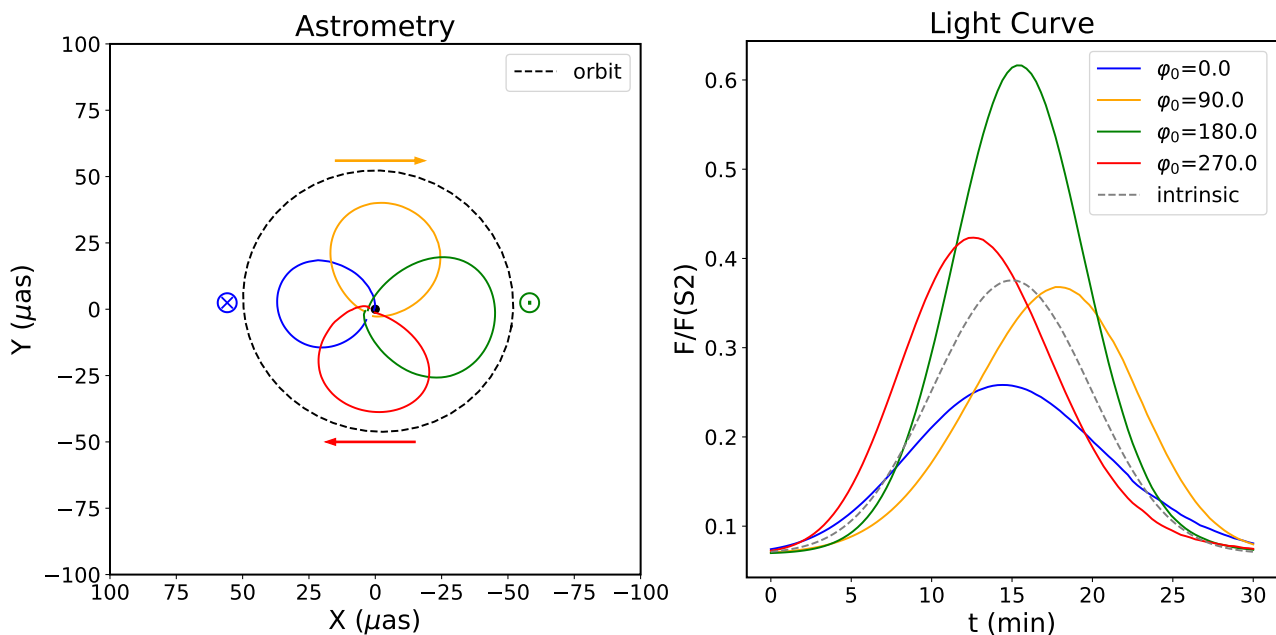


Fig. 4. Astrometry (left) and light curves (right) of the hot spot - jet model for four initial azimuthal angle φ_0 of 0° in blue, 90° in orange, 180° in green and 270° in red. The dashed black line shows the primary image centroid track with no quiescent jet (clock-wise). The jet dominates the beginning and the end of the flares. The observed centroids thus start and end close to the one of the jet. The apparent orbits rotate around the latter with φ_0 as the maximum of emission occurs at different φ . The Gaussian modulation which has a typical duration of $t_\sigma = 15$ min (grey dashed line; which is the same for the four the curves) is affected by relativistic effects. For negative X (right part of the astrometry), the beaming, combined with relativistic Doppler effect, amplify the flux from the hot spot while in the positive X (left part of the figure), they lower it. The black dot in the left panels represents the position of Sgr A*.

but this applies to collisional environments, thus less similar to Sgr A* vicinity.

Fresh plasma flows into the current sheet at the reconnection rate v_{rec} , is accelerated by the electric field generated in the current sheet, usually giving rise to power-law energy distributions of electrons (Sironi & Spitkovsky 2014; Werner et al. 2018). Inside the current sheet, the particles get trapped in the plasmoids which act as particle reservoirs (Sironi & Spitkovsky 2014) which can merge in a macroscopic magnetic island, that is, a large plasmoid. In Ripperda et al. (2022), magnetic flux dissipation through reconnection last for $\sim 100r_g/c \sim 30$ min and the resulting hot spot orbits for $\sim 500r_g/c \sim 150$ min before it disappears by losing its coherence through interaction with the surrounding flow.

In the global PIC simulation of El Mellah et al. (2022), the authors study magnetic reconnection in the sheath of relativistic jet working with magnetic field loops coupling the BH to the accretion disk. The resulting plasmoids evolve off-plane, propagate away from the BH and are prone to merge with each other to form macroscopic plasmoids susceptible to radiate high amounts of energy under the form of non-thermal radiation. The underlying mechanism, first described by Uzdensky (2005) and de Gouveia dal Pino & Lazarian (2005), relies on the accretion of poloidal magnetic field loops onto a spinning BH. Once the inner footpoint of the loop reaches the BH ergosphere, the magnetic field line experiences strong torques due to the frame dragging effect while its other footpoint on the disk rotates at the local Keplerian speed. Thus, the toroidal component of the magnetic field quickly grows in the innermost regions, propagates upstream along the field line and leads to the opening of the magnetic loop above a certain magnetic loop size. On the outermost closed magnetic field line (called the separatrix), a Y-point appears where plasmoids form and flow away along an

inclined current sheet above the disk (Fig. 5). In the PIC simulations of El Mellah et al. (2022), a cone-shaped reconnecting current sheet forms where vivid particle acceleration takes place. Electrons and positrons pile up into outflowing plasmoids where they cool through synchrotron radiation. This topological configuration where some magnetic field lines anchored in the disk close within the event horizon is coherent with what is seen in resistive GRMHD simulations during the short episodes of flux repulsion which separates different accretion regimes. During approximately $100 r_g/c$, these simulations show an essentially force-free funnel surrounded by merging plasmoids formed in the jet sheath and in the equatorial plane Ripperda et al. (2022); Chashkina et al. (2021).

3.1. Plasmoid model from magnetic reconnection

The aim of this section is to develop a semi-analytic large plasmoid model (which will be named *plasmoid model*), inspired from the reconnection literature reviewed above. The interest of such a model, compared to state-of-the-art GRMHD or GRPIC modeling, is twofold:

- it allows to remain as agnostic as possible regarding the physical conditions close to Sgr A* and encapsulate into a single model a large parameter space;
- it allows to perform simulations within a limited computing time, allowing to explore the large parameter space and compare to astrometric and photometric data.

Our hope is that such a model can not only be fed with the results of more elaborated simulations, but also bring constraints to these simulations by determining what features of the modeling are important in order to explain the data.

The main features of our model are illustrated in Fig. 5, inspired by the recent GRPIC results of El Mellah et al. (2022). Here, we consider a single plasmoid, which is modeled as a sphere of hot plasma with a constant radius. This macroscopic plasmoid is understood as the end product of a sequence of microscopic plasmoid mergers. The spherical geometry is chosen only for simplicity, given that current data are certainly unable to make a difference between various geometries.

3.1.1. Plasmoid motion

We consider that the magnetic reconnection event occurs close to the black hole, and the resulting plasmoid is ejected along the jet sheath (Ripperda et al. 2020; El Mellah et al. 2022). Thus, we define a conical motion (as in Ball et al. (2021)) defined by a constant polar angle $\theta = \theta_0$ and the initial conditions r_0 , θ_0 , φ_0 , v_{r0} , and $v_{\varphi 0}$. The subscript 0 reflects the initial value of a given parameter in Boyer-Lindquist coordinate. As in Ball et al. (2021), we set a constant radial velocity $v_r = v_{r0}$ and the azimuthal velocity is defined through the conservation of the Newtonian angular momentum

$$v_{\varphi}(t) = v_{\varphi 0} \frac{r_0^2}{r(t)^2}. \quad (3)$$

The azimuthal angle is obtained by integrating the previous Eq. 3

$$\varphi(t) = \varphi_0 + r_0^2 \frac{v_{\varphi 0}}{v_r} \left(\frac{1}{r_0} - \frac{1}{r(t)} \right). \quad (4)$$

In the GRPIC simulations performed by El Mellah et al. (2022), the plasmoids are formed in the vicinity of the black hole at the Y-point and are ejected into the black hole magnetosphere, we thus restrict our study to $v_r > 0$.

An important feature of our model is the fact that the initial azimuthal velocity of the plasmoid is naturally super-Keplerian. Indeed, the Y-point, from which the plasmoid is generated, is anchored to the equatorial plane of the accretion flow through the separatrix field line. So it will typically rotate at the Keplerian speed corresponding to the foot point of the line, thus at a velocity higher than the Keplerian velocity corresponding to the initial cylindrical radius of the plasmoid.

3.1.2. Growth and cooling phases

We consider two phases in the lifetime of the plasmoid that aim at modeling the ascending and descending phases of the observed flare light curves:

- during the *growth phase*, which lasts a total time t_{growth} , the plasmoid continuously receives fresh accelerated particles at a constant rate resulting from the merging of microscopic plasmoids from reconnection into our large plasmoid which mix with "old" electrons cooled by synchrotron radiation. The growth time t_{growth} corresponds to the lifetime of the reconnection engine, i.e. the duration of magnetic flux dissipation;
- after $t = t_{\text{growth}}$, the plasmoid enters the *cooling phase*: we assume that magnetic reconnection is quenched and plasmoids no longer merge so injection of fresh plasma stops and the plasmoid cools by emitting synchrotron radiation. We neglect particle escape and adiabatic losses.

The duration of the growth phase is set both by the reconnection rate and the speed at which magnetic flux is advected by the accretion flow into the current sheet. In Parfrey et al. (2015), the accretion of successive magnetic loops of opposite polarity activates this process, with typical duration of transition of the order of $100r_g/c$. This duration is representative of the dissipation of the magnetic flux of one magnetic loop which is set by both the size of the loop and the accretion speed, that the authors fix to $2r_g$ and $c/200$ respectively, and the reconnection rate, fixed by the prescribed resistivity. Resistive GRMHD simulations of magnetically arrested disks (Narayan et al. 2003) bring support to these values (e.g. Ripperda et al. 2020) but fail at reaching reconnection rates realistically high (Bransgrove et al. 2021a). In the more ab initio PIC simulations of El Mellah et al. (2022), the reconnection rate is more realistic ($\sim 10\%$, Sironi & Spitkovsky 2014; Werner et al. 2018) but due to the high computational cost of the simulations, they did not work over duration long enough to model the inward drift of the magnetic footpoints on the disk. As a consequence, the reconnection rate is accurate but the fueling magnetic flux is artificially steady and act as an infinite reservoir over the $\sim 200r_g/c$ covered by the simulation. A coupling between GRMHD, force-free and PIC simulations to jointly describe the disk, the corona and the current sheet respectively is still missing. In this context, we considered duration t_{growth} of the growth phase of the order of $100r_g/c$, corresponding to a typical episode of magnetic flux dissipation set by the two rates at which magnetic flux is advected into the current sheet and dissipated by magnetic reconnection.

3.1.3. Evolution of the electron distribution

Next, we prescribe the emission/absorption mechanism in the plasmoid. Most studies use chosen electron distributions, with analytical prescriptions for their evolution at best. Ball et al. (2021) use a fixed thermal distribution with a linear increase of the number density for the rising part of the light curve and a decrease of the temperature following Eq. D.7 for the cooling. Scepi et al. (2022) use a kappa distribution with an exponential cutoff and a synchrotron cooling break for the plasma emission generating X-ray flares. While their evolution of the plasma parameters (number density, temperature, magnetic field) is more elaborate than in our model, their approximation is valid only while injection and cooling are balanced. When the injection stops, the shape of the electron distribution changes rapidly (see Fig. 6). Here, we choose a different approach by evolving the electron distribution in the plasmoid by solving the kinetic equation

$$\frac{\partial N_e(\gamma, t)}{\partial t} = \frac{\partial}{\partial \gamma} \left(-\dot{\gamma}_{\text{syn}} N_e(\gamma, t) \right) + Q_{\text{inj}}(\gamma), \quad (5)$$

where γ is the Lorentz factor of the electrons, Q_{inj} is the injection rate and $N_e = dn_e/d\gamma$ is the electron number density distribution, using the EMBLEM code (Dmytriiev et al. 2021). The term

$$-\dot{\gamma}_{\text{syn}} N_e = \frac{4\sigma_T U_B}{3m_e c} (\gamma^2 - 1) N_e \quad (6)$$

of the right hand side describes the synchrotron cooling of the plasmoid particles, with $U_B = B^2/(8\pi)$. In our approach, we do not model the details of the magnetic reconnection process but instead describe the supply of freshly accelerated particles to the plasmoid by magnetic reconnection. Therefore, for the injection rate $Q_{\text{inj}}(\gamma)$ in Eq. 5, we use the following expression, assuming

non-thermal electrons, i.e. using a thermal distribution, with a linear increase of the number density with a fixed temperature during the growth phase and an analytical prescription for the temperature decrease during the cooling phase using Eq. D.7 and assuming $\Theta_e = \gamma/3$. While this model gives a similar intrinsic light curve as our model, the dimensionless temperature required is twice as high as ours ($\Theta_e = 109$) with a magnetic field of $B = 20$ G to cool faster lower energy electrons. The evolution of the distribution with this model is shown in the bottom left panel of Fig. 6. We do not need such high a temperature as most of the emission comes from high-energy electrons which are non-thermal in our model as suggested by PIC simulations (Rowan et al. 2017; Werner et al. 2018; Ball et al. 2018; Zhang et al. 2021). Our temperature could be even lower with a harder (i.e. lower) κ -index. The cooling of the electron distribution through synchrotron radiation is difficult to model properly and needs a kinetic approach as we do in our plasmoid model.

3.3. Comparing GRAVITY 2018 flare data with our plasmoid model

This paper aims at checking whether we can reproduce with our plasmoid model the general features of the observed light curve and astrometry of the July 22, 2018 flare reported by Gravity Collaboration et al. (2018). We show in Fig. 8 a comparison between the July 22, 2018 flare data observed by GRAVITY (in black) and our plasmoid model (red line) with the parameters listed in Tables 3 and 4. For comparison, we show the intrinsic light curve (dashed line) obtained by removing all the relativistic effects (Doppler effect, beaming, secondary image).

This comparison is not the result of a fit and was obtained by estimating the relevant parameters using simple physical arguments:

- The rise time and slope of the light curve are mainly monitored by (i) the growth time, (ii) our choice of linear evolution of the electron density (which enters the injection function), (iii) the relativistic beaming effect, and thus (iv) the initial azimuthal position of the plasmoid, φ_0 , which has a strong impact on beaming as illustrated in the right panel of Fig. 4.
- The decaying part of the light curve is monitored by the synchrotron cooling time, thus by the magnetic field strength, and by the beaming effect.
- The maximum of the light curve can be estimated by means of an analytical formula that we derive in Appendix C.2. This maximum depends mainly on the maximum number density $n_{e,max}$, as well as on the temperature and κ -index of the distribution. These parameters are degenerate and thus not constrained with only the NIR flare data. Nevertheless, GRMHD (Dexter et al. 2020b; Ripperda et al. 2022; Scepi et al. 2022) and GRPIC simulations (El Mellah et al. 2022) of magnetic reconnection suggest that the density in the plasmoid is higher than its close environment in the current sheet, of the order of the density at the base of the jet, close to the event horizon, but lower than in the disk. Still, the two remaining parameters (Θ_e , κ) which describe the shape of the distribution are fully degenerate.
- The initial position and velocity of the plasmoid have a strong impact on the astrometric trace on sky. We guess the initial azimuthal velocity based on the following reasoning. The Keplerian velocity of the plasmoid at its initial cylindrical radius is $v_{Kep} \sim 0.31c$ (for our choice of initial cylindrical radius given in Table 4, $r_{cyl} = 10.6 r_g$). However, as

Parameter	Symbol	Value
Plasmoid		
magnetic field [G]	B_p	15
plasmoid radius [r_g]	R_p	1
minimal Lorentz factor	γ_{min}	1
maximum Lorentz factor	γ_{max}	10^6
kappa distribution index	κ	4.0
kappa distribution temperature	Θ_e	50
maximum electron number density [cm^{-3}]	$n_{e,max}$	5×10^6
growth timescale [r_g/c]	t_{growth}	120

Table 3. Input parameters of the EMBLEM code for the simulation of the electron distribution evolution. These parameters are used for the July 22 flare of Gravity Collaboration et al. (2018).

Parameter	Symbol	July 22
Plasmoid		
time in EMBLEM at zero observing time [min]	$t_{obs,0}^{emblem}$	29.6
initial cylindrical radius [r_g]	$r_{cyl,0}$	10.6
polar angle [$^\circ$]	θ	135
initial azimuthal angle [$^\circ$]	φ_0	280
initial radial velocity [c]	$v_{r,0}$	0.01
initial azimuthal velocity [c]	$v_{\varphi,0}$	0.45
X position of Sgr A* [μas]	x_0	0
Y position of Sgr A* [μas]	y_0	0
PALN [$^\circ$]	Ω	160

Table 4. Orbital parameters of the plasmoid model following a conical motion used for the comparison of the July 22, 2018 flares observed by Gravity Collaboration et al. (2018).

discussed in Sect. 3.1, our model naturally leads to a super-Keplerian initial velocity to the plasmoid. Indeed, the plasmoid initial azimuthal velocity is that of the footpoint of the separatrix (see Fig. 5). Based on Fig. 8 of El Mellah et al. (2022), we can determine the radius of the footpoint, r_{fp} , of a separatrix giving rise to a Y point located at a cylindrical radius of $\approx 10 r_g$. We find $r_{fp} = (4.7 \pm 0.5) r_g$, which translates in an orbital velocity $v_{\varphi,0}$ between $0.41c$ and $0.45c$. The upper bound of this interval compares well with the July 22 flare data. We note that this estimate of the initial azimuthal velocity is anchored in the model of El Mellah et al. (2022) and thus depends on their choice of initial condition, in particular on the initial profile of their magnetic field.

We note that the fiducial values proposed in Tables 3 and 4 represent a set of parameters with values that are inspired by numerical simulations of reconnection which reproduce the key observational features of the July 22 flare data. This setup is not unique and is not the result of a fit. We let the exploration of the full parameters space (freeing some fixed/constrained parameters like maximum number density, growth time, inclination) to a future work. Nevertheless, our model disfavor low growth time ($t_{growth} < 50 r_g/c$) for this particular flare.

Overall, our plasmoid model jointly describes the astrometry and the flux variation of the 22 July 2018 flare measured by (Gravity Collaboration et al. 2018) for the first time, considering a model with a specific emission prescription. Magnetic reconnection is thus a viable scenario to explain Sgr A* flares.

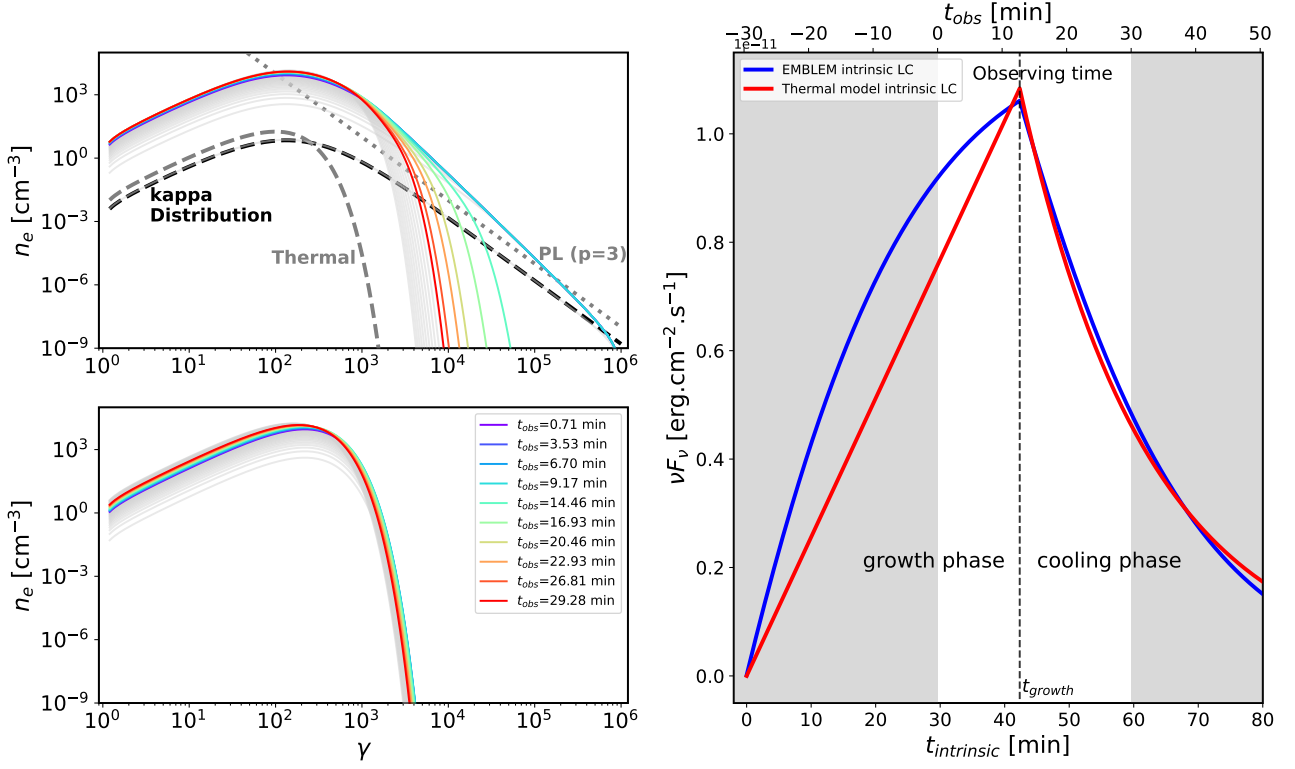


Fig. 6. (Top-left) Evolution of the electron distribution in our model with EMBLEM at each observing time of the July 22, 2018 flare. The black dotted line correspond to the injected κ electron distribution composed of a thermal core with a power law tail. The parameters used are listed in Table 3. (Bottom-left) Evolution of the electron distribution in the Thermal model inspired by Ball et al. (2021) at each observing time of the July 22, 2018 flare. The parameters used for this distribution are the same as in our model (listed in Table 3) but with the dimensionless temperature of $\Theta_e = 109$ and the magnetic field of $B = 20$ G. (Right) Full intrinsic light curves of the two models. Note that in this panel we plot the light curve from the beginning of the growth phase while in the left panels we plot the distribution at the observed time of Fig. 8 ($t_{obs} = t_{intrinsic} - 29.6$ min).

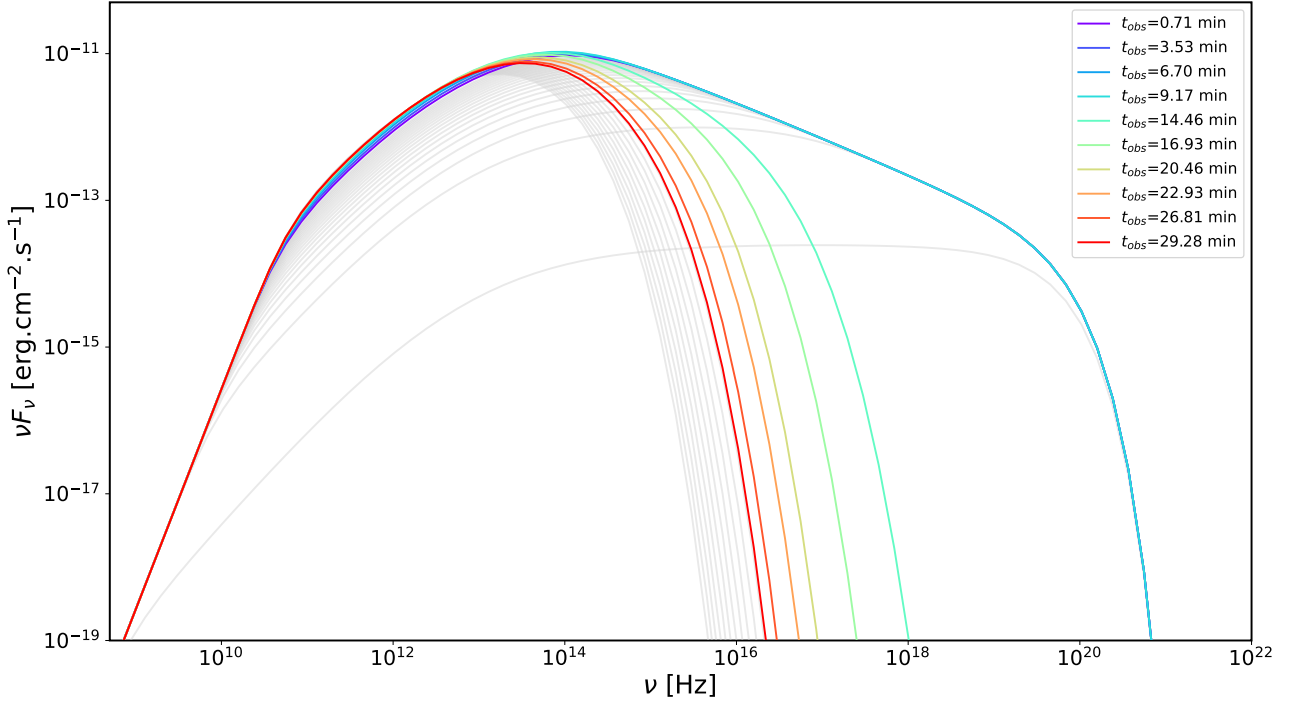


Fig. 7. Intrinsic Spectral Energy Density (SED) evolution from radio to X-rays of our plasmoid model with the parameters listed in Table 3. Color code the time as in Fig. 6. Grey lines are the SED out of the observing time. The SED peak occurs in NIR with this set of parameters, but with a lower κ -index, i.e. a harder power law tail, the peak could reach X-rays. Here, X-rays flux drops quickly compare to the typical timescale of X-ray flares as we consider only synchrotron cooling and not Synchrotron-Self Compton (SSC). We note that the flux emitted by our plasmoid at 230 GHz is ~ 0.1 Jy which is the good order of magnitude of the variability associated to flares in sub-mm (Wielgus et al. 2022a).

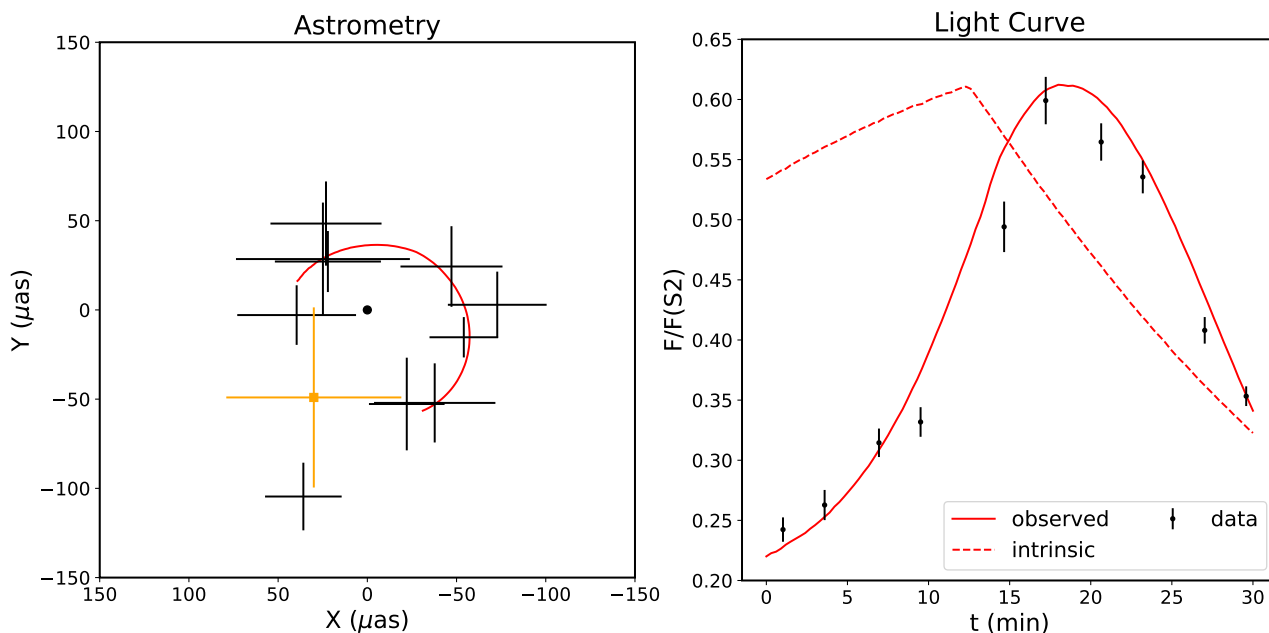


Fig. 8. Data and plasmoid models of the flares from July 22, 2018. The left panels shows the astrometry of the flare while the right panel shows the observed (full line) and intrinsic (dashed line) light curves. The parameters of the model are listed in Tables 3 and 4. Note that this is not the result of a fit. The black dot in the left panels represents the position of Sgr A* in GYOTO and the orange cross represent the position of Sgr A* measured through the orbit of S2.

4. Limitations of our plasmoid model

Our plasmoid model is vastly simplified with respect to the complexity of realistic magnetic reconnection events in the environment of black holes. We review here its main limitations:

- i. We consider a single plasmoid while the instability of thin current sheets gives rise to a dynamic flow of merging magnetic islands. Our argument for this simplification is that the merging process is certainly very dependent on the unknown initial conditions, and that the final, bigger and brighter product of the cascade is likely to dominate the observed signal;
- ii. The initial condition on the plasmoid's velocity is simply imposed for the radial motion, and based on a particular GRPIC model as regards the azimuthal motion;
- iii. The evolution of the plasma parameters (density, temperature, magnetic field) are chosen to be either constant or linear, so very simplified compared to a realistic scenario. However, we consider that these evolutions are very likely to be strongly dependent on the initial conditions of the flow, so that they are weakly constrained;
- iv. The values of almost all the parameters except mass and distance of Sgr A* are poorly constrained. We choose a set of values which are reasonable according to simulations. Future work is needed to investigate the details of the parameter space.
- v. We model the plasmoid by a homogeneous sphere for simplicity from the circle plasmoid seen in 2D GRMHD (Nathanail et al. 2020; Ripperda et al. 2020; Porth et al. 2021) and PIC simulations (Rowan et al. 2017; Ball et al. 2018; Werner et al. 2018). The 3D aspect of such plasmoid is cylindrical (flux ropes) both in GRMHD (Bransgrove et al. 2021b; Nathanail et al. 2022; Ripperda et al. 2022) and PIC (Nättilä & Beloborodov 2021; Zhang et al. 2021) simulations. Thus, a realistic geometry of the flare source is likely more complex than in our model. We note that the exact geometry of the flare is not relevant as we only track the centroid position, as much the flare source is not too extended, and we consider tangled magnetic field. However, the coherence time of the structure might be shorter in 3D and might have an impact on the rise time of the light curve. Further 3D simulations studies are needed to better model the shape of the flux ropes and their evolution;
- vi. We neglect any shearing of the plasmoid and consider that it remains identical to itself throughout the simulation. Differential rotation is however likely to stretch the plasmoid over its orbit and destroy its coherence (Hamaus et al. 2009; Gravity Collaboration et al. 2020c);
- vii. We consider a tangled magnetic field in the plasmoid and thus do not consider the impact of the magnetic field geometry on the observable. The magnetic field geometry of the quiescent flow is likely to be ordered and vertical if Sgr A* is strongly magnetized. The magnetic field in the plasmoid, which is our interest here, could be either helical (plasmoids) or vertical for large flux tubes (Ripperda et al. 2022).
- viii. During a flare, the quiescent state can change in a non axisymmetrical way (Ripperda et al. 2022). This will push the centroid position of the quiescent further away from the center-of-mass location which will affect the offset. We choose to use a static and axisymmetric quiescent model during flare to avoid adding more degrees of freedom which would lead to higher degeneracies, rather than clearer constraints.

ix. We choose a high maximum Lorentz factor $\gamma_{\max} = 10^6$ to be able to power X-ray flares (but without any constrain for this study). However, high energy photons lead to pair-production and thus increase the number density in the plasmoid which we do not take into account.

Despite these many limitations, we consider that our model is very interesting for fitting flare data, because it allows to cover a much broader set of physical scenarios than more elaborate simulations that strongly depend on their assumptions regarding the relevant physics and the initial conditions.

5. Conclusion and perspectives

This paper is mainly focused at developing a new plasmoid model for Sgr A* flares, inspired by magnetic reconnection in black hole environments. Our semi-analytic model allows to study a broad parameter space within a reasonable computing time, thus being well suited for data analysis.

Our model considers non-thermal electrons accelerated by magnetic reconnection and injected into a spherical large plasmoid. We evolve the electron distribution through a kinetic equation taking into account synchrotron cooling and particle injection at a constant rate. We show in Appendix C.1 (Fig. C.3) the importance of taking into account the cooling of the electrons already in plasmoid during the growth phase. Our model also naturally accounts for a super-Keplerian velocity of the flare source, through the dynamical coupling between the plasmoid and the inner regions of the accretion flow through magnetic field lines. One of the main results of this paper is that for the first time we model the astrometry and lightcurve of the flares measured by (Gravity Collaboration et al. 2018) by explicit modeling of the emission zone.

Our conclusions regarding the three main points raised in the introduction are the following:

- the marginally detected shift between the astrometric track of Gravity Collaboration et al. (2018) and the center of mass might be due to the impact of the quiescent radiation of the background accretion flow;
- a dynamical coupling between the plasmoid and the inner accretion flow through closed magnetic field lines might naturally account for the super-Keplerian speed obtained by Gravity Collaboration et al. (2018);
- in general, a large plasmoid due to magnetic reconnection in a thin current sheet in the black hole magnetosphere is a reasonable model to account for the main features of the Gravity Collaboration et al. (2018) observables.

Sect. 3.3 shows that the temperature, density, and κ parameters of the plasmoid are degenerate. This degeneracy might be removed by simultaneous observations of NIR and X-ray flares. Moreover, synchrotron cooling leads to a translation of the electrons from the NIR-emitting band to the millimeter-emitting band, which could explain the sub-mm flare and its time lag with respect to NIR. We thus intend to consider the multi-wavelength properties of our plasmoid model in future work, in order to better assess its ability to account for the complete flare data set of Sgr A*.

A crucial recent observable of Sgr A* flares are the polarization QU loops (Gravity Collaboration et al. 2018, 2020d; Wielgus et al. 2022b). We also intend to study the polarized properties of our plasmoid model and compare it to these recent constraints.

Acknowledgements. NA and FHV are very grateful to B. Cerutti, B. Crinquand, S. von Fellenberg, S. Gillessen, S. Masson, B. Ripperda, N. Scepi, and M. Wielgus for fruitful discussions. This work was granted access to the HPC resources

of MesoPSL financed by the Region Ile de France and the project Equip@Meso (reference ANR-10-EQPX-29-01) of the programme Investissements d’Avenir supervised by the Agence Nationale pour la Recherche.

References

- Backer, D. C. 1978, *ApJ*, 222, L9
- Baganoff, F. K., Bautz, M. W., Brandt, W. N., et al. 2001, *Nature*, 413, 45
- Ball, D., Özel, F., Christian, P., Chan, C.-K., & Psaltis, D. 2021, *ApJ*, 917, 8
- Ball, D., Sironi, L., & Özel, F. 2018, *ApJ*, 862, 80
- Barrière, N. M., Tomsick, J. A., Baganoff, F. K., et al. 2014, *ApJ*, 786, 46
- Bower, G. C., Dexter, J., Asada, K., et al. 2019, *ApJ*, 881, L2
- Bower, G. C., Goss, W. M., Falcke, H., Backer, D. C., & Lithwick, Y. 2006, *ApJ*, 648, L127
- Bower, G. C., Markoff, S., Dexter, J., et al. 2015, *ApJ*, 802, 69
- Bransgrove, A., Ripperda, B., & Philippov, A. 2021a, *Phys. Rev. Lett.*, 127, 055101
- Bransgrove, A., Ripperda, B., & Philippov, A. 2021b, *Phys. Rev. Lett.*, 127, 055101
- Brinkerink, C. D., Falcke, H., Law, C. J., et al. 2015, *A&A*, 576, A41
- Broderick, A. E. & Loeb, A. 2006, *MNRAS*, 367, 905
- Chashkina, A., Bromberg, O., & Levinson, A. 2021, *MNRAS*, 508, 1241
- Chiaberge, M. & Ghisellini, G. 1999, *MNRAS*, 306, 551
- Crinquand, B., Cerutti, B., Dubus, G., Parfrey, K., & Philippov, A. 2021, *A&A*, 650, A163
- Davelaar, J., Mościbrodzka, M., Bronzwaer, T., & Falcke, H. 2018, *A&A*, 612, A34
- de Gouveia dal Pino, E. M. & Lazarian, A. 2005, *A&A*, 441, 845
- Dermer, C. D. & Schlickeiser, R. 2002, *ApJ*, 575, 667
- Dexter, J., Jiménez-Rosales, A., Ressler, S. M., et al. 2020a, *MNRAS*, 494, 4168
- Dexter, J., Tchekhovskoy, A., Jiménez-Rosales, A., et al. 2020b, *MNRAS*, 497, 4999
- Dmytriiev, A., Sol, H., & Zech, A. 2021, *Monthly Notices of the Royal Astronomical Society*, 505, 2712
- Do, T., Ghez, A. M., Morris, M. R., et al. 2009, *ApJ*, 691, 1021
- Do, T., Witzel, G., Gautam, A. K., et al. 2019, *ApJ*, 882, L27
- Dodds-Eden, K., Gillessen, S., Fritz, T. K., et al. 2011, *ApJ*, 728, 37
- Dodds-Eden, K., Porquet, D., Trap, G., et al. 2009, *ApJ*, 698, 676
- Eckart, A., Baganoff, F. K., Morris, M. R., et al. 2009, *A&A*, 500, 935
- Eckart, A., Schödel, R., García-Marín, M., et al. 2008, *A&A*, 492, 337
- Eisenhauer, F., Perrin, G., Brandner, W., et al. 2011, *The Messenger*, 143, 16
- Eisenhauer, F., Perrin, G., Rabien, S., et al. 2008, in *The Power of Optical/IR Interferometry: Recent Scientific Results and 2nd Generation*, ed. A. Richichi, F. Delplancke, F. Paresce, & A. Chelli, 431
- El Mellah, I., Cerutti, B., Crinquand, B., & Parfrey, K. 2022, *A&A*, 663, A169
- Event Horizon Telescope Collaboration, Akiyama, K., Alberdi, A., et al. 2022a, *ApJ*, 930, L12
- Event Horizon Telescope Collaboration, Akiyama, K., Alberdi, A., et al. 2022b, *ApJ*, 930, L16
- Falcke, H. 1999, in *Astronomical Society of the Pacific Conference Series*, Vol. 186, *The Central Parsecs of the Galaxy*, ed. H. Falcke, A. Cotera, W. J. Duschl, F. Melia, & M. J. Rieke, 113
- Fazio, G. G., Hora, J. L., Witzel, G., et al. 2018, *ApJ*, 864, 58
- Genzel, R., Eisenhauer, F., & Gillessen, S. 2010, *Reviews of Modern Physics*, 82, 3121
- Genzel, R., Schödel, R., Ott, T., et al. 2003, *Nature*, 425, 934
- Ghez, A. M., Wright, S. A., Matthews, K., et al. 2004, *ApJ*, 601, L159
- Gravity Collaboration, Abuter, R., Accardo, M., et al. 2017, *A&A*, 602, A94
- GRAVITY Collaboration, Abuter, R., Aymar, N., et al. 2022, *A&A*, 657, L12
- Gravity Collaboration, Abuter, R., Amorim, A., et al. 2020a, *A&A*, 638, A2
- Gravity Collaboration, Abuter, R., Amorim, A., et al. 2020b, *A&A*, 636, L5
- Gravity Collaboration, Abuter, R., Amorim, A., et al. 2018, *A&A*, 618, L10
- Gravity Collaboration, Bauböck, M., Dexter, J., et al. 2020c, *A&A*, 635, A143
- Gravity Collaboration, Jiménez-Rosales, A., Dexter, J., et al. 2020d, *A&A*, 643, A56
- Guo, F., Liu, Y.-H., Daughton, W., & Li, H. 2015, *ApJ*, 806, 167
- Hamaus, N., Paumard, T., Müller, T., et al. 2009, *ApJ*, 692, 902
- Hora, J. L., Witzel, G., Ashby, M. L. N., et al. 2014, *ApJ*, 793, 120
- Hornstein, S. D., Matthews, K., Ghez, A. M., et al. 2007, *ApJ*, 667, 900
- Komissarov, S. S. 2004, *MNRAS*, 350, 427
- Komissarov, S. S. 2005, *MNRAS*, 359, 801
- Komissarov, S. S. & McKinney, J. C. 2007, *MNRAS*, 377, L49
- Krichbaum, T. P., Graham, D. A., Witzel, A., et al. 1998, *A&A*, 335, L106
- Liu, H. B., Wright, M. C. H., Zhao, J.-H., et al. 2016, *A&A*, 593, A44
- Lo, K. Y., Schilizzi, R. T., Cohen, M. H., & Ross, H. N. 1975, *ApJ*, 202, L63
- Loureiro, N. F., Schekochihin, A. A., & Cowley, S. C. 2007, *Physics of Plasmas*, 14, 100703

- Macquart, J.-P., Bower, G. C., Wright, M. C. H., Backer, D. C., & Falcke, H. 2006, *ApJ*, 646, L111
- Marrone, D. P., Baganoff, F. K., Morris, M. R., et al. 2008, *ApJ*, 682, 373
- Marrone, D. P., Moran, J. M., Zhao, J.-H., & Rao, R. 2006, in *Journal of Physics Conference Series*, Vol. 54, *Journal of Physics Conference Series*, 354–362
- Mauerhan, J. C., Morris, M., Walter, F., & Baganoff, F. K. 2005, *ApJ*, 623, L25
- Michail, J. M., Wardle, M., Yusef-Zadeh, F., & Kunneriath, D. 2021a, *ApJ*, 923, 54
- Michail, J. M., Yusef-Zadeh, F., & Wardle, M. 2021b, *MNRAS*, 505, 3616
- Mościbrodzka, M. & Falcke, H. 2013, *A&A*, 559, L3
- Narayan, R., Igumenshchev, I. V., & Abramowicz, M. A. 2003, *PASJ*, 55, L69
- Nathanail, A., Fromm, C. M., Porth, O., et al. 2020, *MNRAS*, 495, 1549
- Nathanail, A., Mpisketzi, V., Porth, O., Fromm, C. M., & Rezzolla, L. 2022, *MNRAS*, 513, 4267
- Nättilä, J. & Beloborodov, A. M. 2021, *ApJ*, 921, 87
- Nayakshin, S., Cuadra, J., & Sunyaev, R. 2004, *A&A*, 413, 173
- Neilsen, J., Nowak, M. A., Gammie, C., et al. 2013, *ApJ*, 774, 42
- Nowak, M. A., Neilsen, J., Markoff, S. B., et al. 2012, *ApJ*, 759, 95
- Pandya, A., Zhang, Z., Chandra, M., & Gammie, C. F. 2016, *ApJ*, 822, 34
- Parfrey, K., Giannios, D., & Beloborodov, A. M. 2015, *MNRAS*, 446, L61
- Parfrey, K., Philippov, A., & Cerutti, B. 2019, *Phys. Rev. Lett.*, 122, 035101
- Paumard, T., Perrin, G., Eckart, A., et al. 2008, in *The Power of Optical/IR Interferometry: Recent Scientific Results and 2nd Generation*, ed. A. Richichi, F. Delplancke, F. Paresce, & A. Chelli, 313
- Paumard, T., Vincent, F. H., Straub, O., & Lamy, F. 2019, *Gyoto*
- Ponti, G., De Marco, B., Morris, M. R., et al. 2015, *MNRAS*, 454, 1525
- Porth, O., Chatterjee, K., Narayan, R., et al. 2019, *ApJS*, 243, 26
- Porth, O., Mizuno, Y., Younsi, Z., & Fromm, C. M. 2021, *MNRAS*, 502, 2023
- Ressler, S. M., Tchekhovskoy, A., Quataert, E., & Gammie, C. F. 2017, *MNRAS*, 467, 3604
- Ripperda, B., Bacchini, F., & Philippov, A. A. 2020, *ApJ*, 900, 100
- Ripperda, B., Liska, M., Chatterjee, K., et al. 2022, *ApJ*, 924, L32
- Rowan, M. E., Sironi, L., & Narayan, R. 2017, *ApJ*, 850, 29
- Rybicki, G. B. & Lightman, A. P. 1979, *Radiative processes in astrophysics*
- Rybicki, G. B. & Lightman, A. P. 1986, *Radiative Processes in Astrophysics*
- Scepi, N., Dexter, J., & Begelman, M. C. 2022, *MNRAS*, 511, 3536
- Sironi, L. & Spitkovsky, A. 2014, *ApJ*, 783, L21
- Tagger, M. & Melia, F. 2006, *ApJ*, 636, L33
- Uzdensky, D. A. 2005, *ApJ*, 620, 889
- Vincent, F. H., Abramowicz, M. A., Zdziarski, A. A., et al. 2019, *A&A*, 624, A52
- Vincent, F. H., Paumard, T., Gourgoulhon, E., & Perrin, G. 2011, *Classical and Quantum Gravity*, 28, 225011
- Vincent, F. H., Paumard, T., Perrin, G., et al. 2014, *MNRAS*, 441, 3477
- von Fellenberg, S. D., Gillessen, S., Graciá-Carpio, J., et al. 2018, *ApJ*, 862, 129
- Werner, G. R., Uzdensky, D. A., Begelman, M. C., Cerutti, B., & Nalewajko, K. 2018, *MNRAS*, 473, 4840
- Wielgus, M., Marchili, N., Martí-Vidal, I., et al. 2022a, *ApJ*, 930, L19
- Wielgus, M., Moscibrodzka, M., Vos, J., et al. 2022b, *A&A*, 665, L6
- Witzel, G., Martinez, G., Hora, J., et al. 2018, *ApJ*, 863, 15
- Witzel, G., Martinez, G., Willner, S. P., et al. 2021, *ApJ*, 917, 73
- Yusef-Zadeh, F., Roberts, D., Wardle, M., Heinke, C. O., & Bower, G. C. 2006, *ApJ*, 650, 189
- Zhang, H., Sironi, L., & Giannios, D. 2021, *ApJ*, 922, 261

Appendix A: Torus - Jet model for the quiescent state

We used the Torus-jet model of Vincent et al. (2019). Their jet model is restricted to an emitting sheath with an empty funnel in agreement with GRMHD simulations (e.g. Mościbrodzka & Falcke 2013; Ressler et al. 2017; Davelaar et al. 2018; Porth et al. 2019). In their model, Vincent et al. (2019) define an opening and closing angle θ_1 and θ_2 respectively and a base height z_b to define the geometry of the jet. The number density and the temperature are defined by their values at the base height of the jet (n_e^J and T_e^J respectively) and their profiles along the jet. The profile of the number density is fixed ($\propto r_{cyl}^{-2}$ with r_{cyl} the projected radius in the equatorial plane) and the one of the temperature is set by the temperatures slope s_T ($\propto z^{-s_T}$ with z the height along the vertical/spin axis). The jet emits synchrotron radiation from a κ electron distribution.

The torus is defined by its central density and temperature (n_e^T and T_e^T respectively). The profiles of these two quantities in the torus are governed by the polytropic index k and its geometry. The latter is defined by the inner radius r_{in} and the angular momentum l but also on the metric (see Vincent et al. (2019) for more details). Contrary to the jet, we consider that the electron distribution of the torus is purely thermal.

We use the same algorithm as in Vincent et al. (2019) after the correction of a small technical issue leading to an overestimation of the number density and temperature. However, we change the choice of the magnetization parameter in the jet sheath. As illustrated e.g. by Porth et al. (2019), the jet sheath, which corresponds to the dominating emission region of the jet, coincides with the transition between the highly-magnetized ($\sigma \gg 1$) funnel and the less-magnetized ($\sigma \ll 1$) main disk body. Consequently, we fix the magnetization to $\sigma = 1$ in the emitting jet sheath, while Vincent et al. (2019) used a low magnetization both in the jet and in the torus. Our choice leads to a smaller density in the jet sheath compared to Vincent et al. (2019). We found a best-fit with a $\chi_{red}^2 = 0.91$ using the same data points as Vincent et al. (2019). The values are reported in Table 1 and Fig. 2 shows the associated spectrum and the image at $2.2 \mu m$. We obtain a magnetic field strength of 257 G for the jet and 212 G at the center of the torus. These values are higher than in Bower et al. (2019) who considers a full thermal electron population with a higher temperature but are of the same order as in Scepi et al. (2022).

Appendix B: Ray-tracing setup

We consider a Kerr black hole with dimensionless spin parameter $a = 0$, described in Boyer-Lindquist (t, r, θ, φ) coordinates. We work in units where the gravitational constant and the speed of light are equal to 1, $G = c = 1$. Radii are thus expressed in units of the black hole mass M .

We use the backward ray-tracing code GYOTO³ (Vincent et al. 2011; Paumard et al. 2019) to compute images of our models at different epochs. Each pixel of our image corresponds to a direction on sky. For each pixel of the image (i.e. each direction), a null geodesic is integrated backwards in time from the observer towards the black hole, integrating along this path the radiative transfer equation

$$\frac{dI_\nu}{ds} = -\alpha_\nu I_\nu + j_\nu \quad (\text{B.1})$$

³ <https://gyoto.obspm.fr>

using the synchrotron emissivity j_ν and absorptivity α_ν coefficients, considering various electron distribution functions. This allows us to determine the flux centroid for each epoch and trace its motion. In addition to astrometry we also determine the total flux emitted as the sum of the intensity weighted by the element of solid angle subtended by each pixel, again, for each epoch which allows us to plot the light curve.

The images produced are 1000x1000 pixels with a field of view of $300 \mu as$ vertically and horizontally which makes a resolution $< 0.1 \mu as^2/pixel$. This high resolution is needed to resolve properly the secondary image which has a very important role in both astrometry and light curve (see Sect. 2).

We model the quiescent state of Sgr A* at $2.2 \mu m$ with a jet (see Sect. 2.1). However, computing an image of the jet is ~ 200 times longer than an image of the flare source (i.e. the hot spot or the plasmoid, Sect. 2 and 3 respectively) because the jet is much more extended, and integrating the radiative transfer equation is thus much longer. The absorption in the jet is negligible thus the flux emitted by the flare which crosses the jet is fully transmitted. We can compute a single image of the jet that we add to each images of the hot spot a posteriori. We then calculate the total flux by summing the jet flux with the one of the flare at a given time. The final centroid position is calculated by a simple barycenter of the two centroids (jet and flare).

Appendix C: Intrinsic emission of the Plasmoid

Appendix C.1: Tests on the kinetic simulations

In our model, we follow the evolution of the electron distribution taking into account the injection of accelerated electrons by the merging of small plasmoids into our large plasmoid and their cooling through synchrotron radiation. The emissivity j_ν and absorptivity α_ν coefficients, needed to integrate the radiative transfer Eq. B.1, are computed through the formula of Chiaberge & Ghisellini (1999); Rybicki & Lightman (1986) (with our notation)

$$j_\nu(t) = \frac{1}{4\pi} \int_{\gamma_{min}}^{\gamma_{max}} d\gamma N_e(\gamma, t) P_s(\nu, \gamma), \quad (\text{C.1})$$

$$\alpha_\nu(t) = -\frac{1}{8\pi m_e \nu^2} \int_{\gamma_{min}}^{\gamma_{max}} \frac{N_e(\gamma, t)}{\gamma l} \frac{d}{d\gamma} [\gamma l P_s(\nu, \gamma)] \quad (\text{C.2})$$

with

$$P_s(\nu, \gamma) = \frac{3\sqrt{3}}{\pi} \frac{\sigma_T c U_B}{\nu_B} x^2 \left\{ K_{4/3}(x) K_{1/3}(x) - \frac{3}{5} x [K_{4/3}^2(x) - K_{1/3}^2(x)] \right\} \quad (\text{C.3})$$

where $l = (\gamma^2 - 1)^{1/2}$ is the electron momentum in units of $m_e c$, $x = \nu / (3\gamma^2 \nu_B)$, $\nu_B = eB / (2\pi m_e c)$ and $K_a(t)$ is the modified Bessel function of order a . We note that the Eq. C.3, is already averaged over pitch angle. For standard distributions as thermal, power-law and κ -distributions, these formulae are equivalent to the fits of Pandya et al. (2016) (see Appendix D) that we used for computing the quiescent synchrotron flux.

As electrons start to cool as soon as they are injected in the plasmoid, the full distribution is no more a κ -distribution. However, turning off the cooling during the growth phase allows us to compare the results of EMBLEM to the fitting formulae of Pandya et al. (2016). As we inject electrons following their definition of

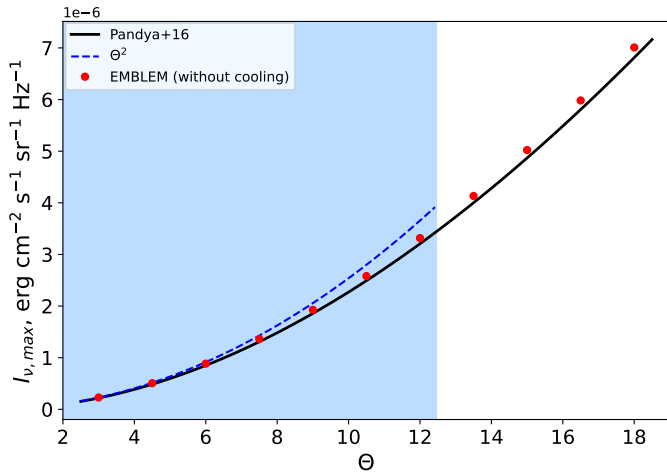


Fig. C.1. Specific intensity at the end of the growth phase ($t = t_{\text{growth}} = 75 r_g/c$) of a κ -distribution with $n_e = 5 \times 10^6 \text{ cm}^{-3}$, $B = 10 \text{ G}$, $\kappa = 4$ for a range of Θ_e computed from the full fitting formulae of Pandya et al. (2016) (black curve), by the EMBLEM code (red dots) and with the high-frequency limit analytical expression (dashed blue curve). We overplot in light blue the range of Θ_e where $X_{\kappa} > 2000$ i.e. where the relative error between the high frequency limit and the full formula is lower than 20%.

the κ -distribution with a linear increase of the number density, the two approach show similar results (see Appendix D). In our cases, the absorption is very low, thus we neglect the absorption in these tests. We can derive an analytical formula for the specific intensity from the high frequency limit emissivity Eq. D.3 depending on the number density n_e , the electron temperature Θ_e and the magnetic field B in case the cooling is switched off during growth. We find in the case without cooling that, keeping κ constant

$$I_{\nu, \text{max}} \propto n_{e, \text{max}} \Theta^{\kappa-2} B^{\kappa/2}, \text{ if } X_{\kappa} > 2000. \quad (\text{C.4})$$

We show the relative error of the maximum specific intensity between the EMBLEM code (red dots) and the formulae of Pandya et al. (2016) (black curve) depending on the electron temperature and the magnetic field in Fig. C.1 and C.2. We fix the others parameters to $n_e = 5 \times 10^6 \text{ cm}^{-3}$, $\kappa = 4$, $t_{\text{growth}} = 75 r_g/c$. The values of EMBLEM are in good agreement with the previous analytical expression (Eq. C.4) for low values of Θ_e and B . For high values, we are beyond the validity of our approximations (in the intermediate frequency regime of the fitting formula, see Appendix D). Comparing the results of EMBLEM (without cooling) with the full fitting formula of Pandya et al. (2016) (black curves) results in an error lower than 5% showing the good agreement between the two approaches.

Appendix C.2: Analytical estimate of the intrinsic light curve

Next, we compute the light curve emitted by the plasmoid which will be affected by the relativistic effects. To reproduce a given light curve, we can estimate the values of the parameters through characteristic scales. The growth time, which is a "free" parameter of the model, can be estimated from the light curve taking into account the beaming effect and thus, depends on the orbital parameters. The synchrotron cooling time of an electron with Lorentz factor γ in a magnetic field B reads

$$t_{\text{cool}} = \frac{3}{4} \frac{m_e c}{\sigma_T U_B \gamma} \quad (\text{C.5})$$

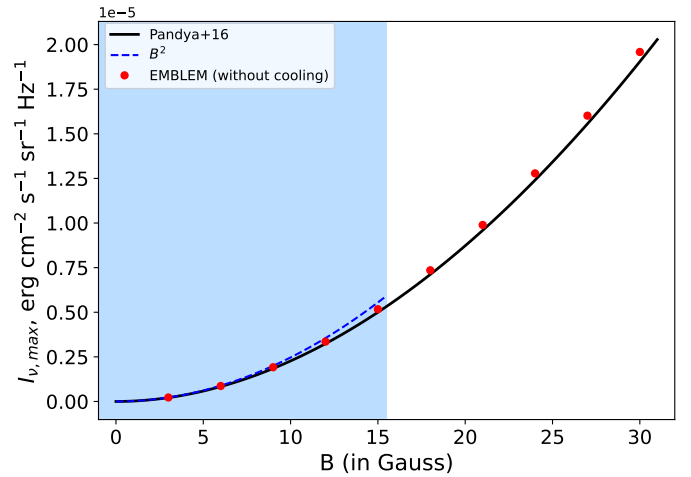


Fig. C.2. Same as in Fig. C.1 for a range of B and with $\Theta_e = 10$.

with σ_T the electron Thomson cross section and U_B the magnetic energy density. In a Dirac spectrum approximation, the Lorentz factor of an electron emitting an IR photon at $2.2 \mu\text{m}$ is (Rybicki & Lightman 1979)

$$\tilde{\gamma} = \left(\frac{\nu m_e c}{\eta e B} \right)^{1/2} \quad (\text{C.6})$$

with $\eta = (0.29 \times 3)/(2\pi)$ a dimensionless numerical factor (see Appendix E.2). One can thus constrain the magnetic field from the synchrotron cooling time as

$$t_{\text{cool}} = 19 \times \left(\frac{B}{20\text{G}} \right)^{-1.5} \left(\frac{\lambda}{2.2\mu\text{m}} \right)^{0.5} \text{ min}. \quad (\text{C.7})$$

Taking into account the cooling of the electrons during the growth phase leads to a lower flux than what we estimate from Eq. C.4. Indeed, as electrons start to cool directly after being injected, the integral of the distribution in Eq. C.1 and so the emissivity will always be lower than without cooling. The key parameter of synchrotron cooling is the cooling time scale (Eq. C.5), which depends on the magnetic field strength and the initial energy of the electrons. It has to be compared to the growth time. Indeed, with a low growth time, only high-energy electrons have the time to cool. Increasing the growth time will allow lower energy electrons to cool and so decrease even more the maximum flux of the light curve.

With some approximations (see Appendix E for the details), one can estimate the flux with cooling at $t = t_{\text{growth}}$

$$\nu F_{\nu}^{\text{syn}}(\nu, t) = \frac{n_e R_b^3 \tilde{\gamma} m_e c^2}{12 D^2 t_{\text{growth}} \kappa \theta^2} \begin{cases} [\Psi(\tilde{\gamma}) - \Psi(\xi(\tilde{\gamma}, t))], & \text{for } \nu < \tilde{\nu}(t) \\ \Psi(\tilde{\gamma}), & \text{for } \nu \geq \tilde{\nu}(t) \end{cases} \quad (\text{C.8})$$

where $\tilde{\nu}(t) = (\eta e B)/(m_e c b_c^2 t^2)$ is the frequency corresponding to the condition $\tilde{\gamma} = 1/(b_c t)$ and

$$\Psi(x) = \left(1 + \frac{x-1}{\kappa \theta} \right)^{-\kappa} \left[x^2(\kappa-1) + 2x(\kappa\theta-1) + 2\theta(\kappa\theta-2) \right]. \quad (\text{C.9})$$

We plot the maximum light curve evolution relative to the magnetic field with EMBLEM with (blue crosses) and without (red

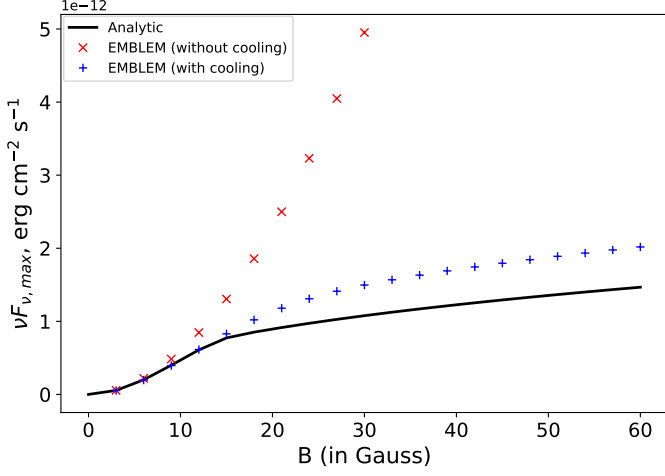


Fig. C.3. Evolution of the maximum flux $\nu F_{\nu}(t_{\text{growth}})$ (at the end of the growth phase $t_{\text{growth}} = 75 r_g/c$) as a function of the magnetic field. We show the results of EMBLEM without cooling (red crosses) as in Fig. C.2. Allowing the cooling during the growth phase results in a lower maximum flux (blue crosses). One can estimate the maximum flux with cooling through Eq. C.8 (see Appendix E for details). This equation is divided in two regimes, the equilibrium regime where the magnetic field is strong enough to compensate the injection and creates a stationary state ($B \geq 16.2$ G) and non stationary regime where not all electrons have cooled at t_{growth} ($B < 16.2$ G). The relative error between the analytical formula and the results of EMBLEM (with cooling) is below 30% in the whole domain and below 7% in the non stationary regime.

crosses) cooling during the growth phase and the previous analytical expression in Fig. C.3 (black line). As expected, the cooling becomes more significant with a strong magnetic field until the maximum flux starts to decrease for very high values ($B > 100$ G). The two regimes of Eq. C.8 are clearly visible in Fig. C.3 with a turning point at $B = 16.2$ G. This approximation has a maximum relative error lower than 30% compared to the results of EMBLEM in the stationary regime and below 7% for the non stationary regime making it a good approximation estimate the peak light curve flux.

Appendix D: Computation of the synchrotron coefficients for the Plasmoid

Appendix D.1: Fitting formulae of Pandya et al. (2016)

In the hot spot model and for the test of EMBLEM, we used the fitting formula of Pandya et al. (2016) to compute the emissivity j_ν and absorptivity α_ν considering a well defined κ -distribution. This distribution has two regimes, the low and high frequency regimes.

In the low frequency limit, the emissivity is

$$j_{\nu,low} = \frac{n_e e^2 \nu_B}{c} X_\kappa^{1/3} \sin(\theta) \frac{4\pi\Gamma(\kappa - 4/3)}{3^{7/3}\Gamma(\kappa - 2)} \quad (\text{D.1})$$

and the absorption coefficient is

$$\alpha_{\nu,low} = \frac{n_e e^2}{\nu m_e c} X_\kappa^{-2/3} 3^{1/6} \frac{10}{41} \frac{2\pi}{(\Theta_e \kappa)^{10/3-\kappa}} \frac{(\kappa - 2)(\kappa - 1)\kappa}{3\kappa - 1} \times \Gamma\left(\frac{5}{3}\right) {}_2F_1\left(\kappa - \frac{1}{3}, \kappa + 1, \kappa + \frac{2}{3}, -\Theta_e \kappa\right) \quad (\text{D.2})$$

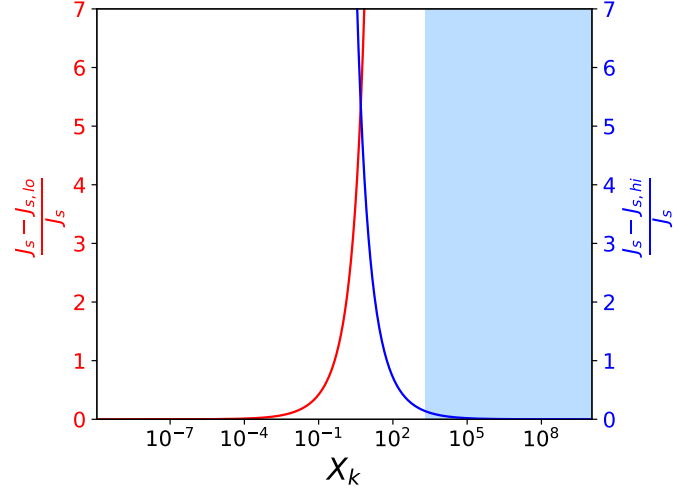


Fig. D.1. Relative error between the low frequency regime (in red) - resp. the high frequency regime (in blue) - fit formulae $J_{s,lo}$ (resp. $J_{s,hi}$) of Pandya et al. (2016) and the full fit formula of the emission coefficient J_s in function of $X_\kappa = \frac{\nu}{\nu_\kappa}$ with $\nu_\kappa = \nu_B (\Theta_e \kappa)^2$.

where ${}_2F_1$ is the hypergeometric function.

In the high-frequency limit, the emissivity is

$$j_{\nu,high} = \frac{n_e e^2 \nu_B}{c} X_\kappa^{-(\kappa-2)/2} \sin(\theta) 3^{(\kappa-1)/2} \times \frac{(\kappa - 2)(\kappa - 1)}{4} \Gamma\left(\frac{\kappa}{4} - \frac{1}{3}\right) \Gamma\left(\frac{\kappa}{4} + \frac{4}{3}\right) \quad (\text{D.3})$$

and the absorption coefficient is

$$\alpha_{\nu,high} = \frac{n_e e^2}{\nu m_e c} X_\kappa^{-(1+\kappa)/2} \frac{\pi^{3/2}}{3} \frac{(\kappa - 2)(\kappa - 1)\kappa}{(\Theta_e \kappa)^3} \times \left(\frac{2\Gamma(2 + \kappa/2)}{2 + \kappa} - 1\right) \left[\left(\frac{3}{\kappa}\right)^{19/4} + \frac{3}{5}\right]. \quad (\text{D.4})$$

The final approximations for the emissivity and absorption coefficient are

$$j_\nu = \left(j_{\nu,low} + j_{\nu,high}\right)^{-1/x_j} \quad (\text{D.5})$$

$$\alpha_\nu = \left(\alpha_{\nu,low} + \alpha_{\nu,high}\right)^{-1/x_\alpha} \quad (\text{D.6})$$

with $x_j = 3\kappa^{-3/2}$ and $x_\alpha = \left(-\frac{7}{4} + \frac{8}{5}\kappa\right)^{-43/50}$.

The two frequency limits do not have the same dependence on the parameters. The frequency regime is defined by the dimensionless parameter $X_\kappa = \nu/\nu_\kappa$, with $\nu_\kappa = \nu_B (\Theta_e \kappa)^2$. Fig. D.1 shows the relative error of the two regimes (the low frequency in red and the high frequency in blue) compared to the final emission coefficient. While at very high (respectively very low) X_κ , the high frequency (resp. low frequency) fitting formulae work very well, there is a large frequency regime ($10^{-2} \leq X_\kappa \leq 10^3$), hereafter *intermediate regime*, where both limits are needed. At $2.2 \mu\text{m}$, $X_\kappa > 1$, while $\Theta_e \kappa \lesssim 10^3$ which correspond to our typical set of parameters. This is why we used the high frequency regime for our test our EMBLEM.

Appendix D.2: Chiaberge & Ghisellini (1999) approximation

Modeling the synchrotron cooling of the electrons with a thermal, power-law or κ distribution is not trivial. Indeed, the evolution of the energy of an electron which emits synchrotron radiation is (e.g., Rybicki & Lightman (1986))

$$\gamma(t) = \gamma_0(1 + A\gamma_0 t)^{-1} \quad (\text{D.7})$$

$$\text{with } A = \frac{4}{3} \frac{\sigma_T B^2}{8\pi m_e c}, \quad (\text{D.8})$$

γ the Lorentz factor of the electron at time t , and γ_0 the initial Lorentz factor. The energy evolution strongly depends on the initial energy. The higher the initial energy of the electron, the faster it will cool. Thus, the initial distribution we could impose will quickly be deformed (see top-left panel of Fig. 6) and could not be modeled by one (or more) of the three distribution of Pandya et al. (2016) (thermal, power-law and/or κ).

In order to properly model the cooling of electrons, we simulate the evolution of the electron distribution with injection and synchrotron cooling (Sect. 3). These simulations give us the electron distribution $N_e(\gamma, t)$ at different times. We compute the emissivity j_ν and the absorptivity α_ν associated for a range of frequencies from 10^6 to 10^{21} Hz following the formula of Chiaberge & Ghisellini (1999) (with our notation)

$$j_\nu(t) = \frac{1}{4\pi} \int_{\gamma_{\min}}^{\gamma_{\max}} d\gamma N_e(\gamma, t) P_s(\nu, \gamma) \quad (\text{D.9})$$

and the absorption coefficient follows

$$\alpha_\nu(t) = -\frac{1}{8\pi m_e \nu^2} \int_{\gamma_{\min}}^{\gamma_{\max}} \frac{N_e(\gamma, t)}{\gamma p} \frac{d}{d\gamma} [\gamma p P_s(\nu, \gamma)], \quad (\text{D.10})$$

where $p = (\gamma^2 - 1)^{1/2}$ is the electron momentum in units of $m_e c$ and P_s is the emissivity of a single electron (see C.3).

In order to obtain the emissivity and absorption coefficient at any time and any frequency (to account the relativistic Doppler effect for example), we made a bilinear interpolation.

Appendix E: Analytical approximation for Sgr A* flare peak flux

Here we derive an analytical expression to compute the time-dependent flux from Sgr A* flares during the growth phase, and obtain an analytical formula for the peak flare flux. For that, we first obtain the approximate analytical form of the varying electron spectrum during the growth phase by solving the kinetic equation, and then compute the approximate synchrotron SED associated to the time-dependent electron spectrum.

Appendix E.1: Deriving time-dependent electron spectrum during the growth phase

The kinetic equation describing the evolution of the electron spectrum during the growth phase is given by Eq. 5:

$$\frac{\partial N_e(\gamma, t)}{\partial t} = \frac{\partial}{\partial \gamma} (b_c \gamma^2 N_e(\gamma, t)) + Q_{\text{inj}}(\gamma, n_e, \theta, \kappa) \quad (\text{E.1})$$

with the injection term $Q_{\text{inj}}(\gamma)$ given by Eq. 7 and Eq. 8, and synchrotron cooling term $\dot{\gamma}_{\text{syn}} = -b_c(\gamma^2 - 1)$ (see Eq. 6), where

$b_c = (4\sigma_T U_B)/(3m_e c)$. We use here an approximation $\dot{\gamma}_{\text{syn}} \approx -b_c \gamma^2$, as the bulk of the electrons producing the flare emission are highly relativistic.

We use the method of characteristics to solve the kinetic equation. We search for characteristic curves in the γ - t space, along which our differential equation in partial derivatives becomes an ordinary differential equation. Let us rewrite the kinetic equation in the following form, expanding the derivative on the Lorentz factor:

$$\frac{\partial N_e(\gamma, t)}{\partial t} + (-1)b_c \gamma^2 \frac{\partial N_e(\gamma, t)}{\partial \gamma} = Q_{\text{inj}}(\gamma) + 2\gamma b_c N_e(\gamma, t) \quad (\text{E.2})$$

When restricting our equation to the characteristic curve $(\gamma(t), t)$, the full derivative of the electron spectrum over time, by the chain rule, is:

$$\frac{dN_e(\gamma, t)}{dt} = \frac{\partial N_e(\gamma, t)}{\partial t} + \frac{d\gamma}{dt} \frac{\partial N_e(\gamma, t)}{\partial \gamma} \quad (\text{E.3})$$

Comparing this to Eq. E.2, we identify $(-1)b_c \gamma^2 = \frac{d\gamma}{dt}$, and therefore along the chosen characteristic curve, our equation is split into a system of two ordinary differential equations:

$$\begin{cases} d\gamma/dt = -b_c \gamma^2 \\ dN_e(\gamma, t)/dt = Q_{\text{inj}}(\gamma) + 2\gamma b_c N_e(\gamma, t) \end{cases} \quad (\text{E.4})$$

The solution of the first equation is (applying the initial condition that $\gamma(t=0) = \xi$):

$$\gamma(t) = \frac{1}{b_c t + 1/\xi} \quad (\text{E.5})$$

This equation defines a characteristic curve in the γ - t space. We have chosen the initial point of the characteristic curve as $(\xi, 0)$. The physical meaning of ξ is the initial value of the Lorentz factor of an electron before it starts undergoing the cooling process. Eq. E.5 is equivalent to Eq. D.7, and describes how the Lorentz factor of an individual electron evolves in time due to synchrotron cooling. From this equation, the initial Lorentz factor ξ is:

$$\xi = \xi(\gamma, t) = \frac{1}{1/\gamma - b_c t} \quad (\text{E.6})$$

This formula defines the initial Lorentz factor of the characteristic curve that passes through a point (γ, t) . We denote the function $N_e(\gamma_\xi(t), t) = u(t)$ (electron spectrum along the characteristic curve), and solve the second equation in the system:

$$du/dt - 2b_c \gamma(t)u = Q_{\text{inj}}(\gamma(t)) \quad (\text{E.7})$$

The generic solution of this linear differential equation is:

$$u(t) = \frac{1}{\mu(t)} \int_0^t \mu(t') Q_{\text{inj}}(\gamma(t')) dt' + \frac{C}{\mu(t)} \quad (\text{E.8})$$

with C being the integration constant, and the function $\mu(t)$ being the integration factor, which is equal to:

$$\mu(t) = \exp\left(\int -2b_c\gamma(t)dt\right) = \frac{1}{(b_c t + 1/\xi)^2} \quad (\text{E.9})$$

As the electron spectrum at $t = 0$ is zero, we set the initial condition $u(t = 0) = 0$, which results in $C = 0$. Therefore, the solution for $u(t)$ is:

$$u(t) = (b_c t + 1/\xi)^2 \int_0^t (b_c t' + 1/\xi)^{-2} Q_{\text{inj}}(\gamma(t')) dt' \quad (\text{E.10})$$

Now we have to return back from $u(t)$ to $N_e(\gamma, t)$, which is achieved by substitution of the equation for $\xi = \xi(\gamma, t)$ (Eq. E.6) to the expression for $u(t)$. After doing that, we obtain an expression for the electron spectrum at a moment of time t :

$$N_e(\gamma, t) = \frac{1}{\gamma^2} \int_0^t \Gamma^2 Q_{\text{inj}}(\Gamma) dt' \quad (\text{E.11})$$

with $\Gamma = \Gamma(\gamma, t, t') = [1/\gamma + b_c(t' - t)]^{-1}$. We use here an approximation for $Q_{\text{inj}}(\Gamma)$, and more specifically, for the kappa distribution, to enable analytical integration. As we are in the relativistic regime, and the peak of the injection spectrum in our case typically occurs at Lorentz factors $\gamma \gg 1$, we can substitute $\gamma(\gamma^2 - 1)^{1/2}$ with γ^2 in the Eq. 8. This leads to some inaccuracies only at very low Lorentz factors, which virtually do not contribute to the integral value, and do not contribute to the light curve flux. We therefore use for the injected spectrum:

$$Q_{\text{inj}}(\gamma, n_e, \theta, \kappa) \approx \frac{N}{t_{\text{growth}}} \gamma^2 \left(1 + \frac{\gamma - 1}{\kappa\theta}\right)^{-(\kappa+1)} \quad (\text{E.12})$$

Now we can perform the analytical integration. We use the variable substitution from t' to $\Gamma(\gamma, t, t')$. In this case, the differential $dt' = -b_c^{-1}\Gamma^{-2}d\Gamma$. Our integral (Eq. E.11) then becomes:

$$\begin{aligned} N_e(\gamma, t) &= \frac{N}{\gamma^2 t_{\text{growth}}} \int_0^t \Gamma^4 \left(1 + \frac{\Gamma - 1}{\kappa\theta}\right)^{-(\kappa+1)} dt' = \\ &= -\frac{N}{b_c \gamma^2 t_{\text{growth}}} \int_0^t \Gamma^2 \left(1 + \frac{\Gamma - 1}{\kappa\theta}\right)^{-(\kappa+1)} d\Gamma \quad (\text{E.13}) \end{aligned}$$

To solve the integral, we perform integration by parts, and we obtain:

$$\int_0^t \Gamma^2 \left(1 + \frac{\Gamma - 1}{\kappa\theta}\right)^{-(\kappa+1)} d\Gamma = -\frac{\theta\kappa}{(\kappa - 2)(\kappa - 1)} \Psi(\Gamma) \Big|_0^t \quad (\text{E.14})$$

with

$$\Psi(x) = \left(1 + \frac{x - 1}{\kappa\theta}\right)^{-\kappa} \left[x^2(\kappa - 1) + 2x(\kappa\theta - 1) + 2\theta(\kappa\theta - 2)\right] \quad (\text{E.15})$$

We substitute the variable back from Γ to t' , with $\Gamma(t' = 0) = (1/\gamma - b_c t)^{-1} = \xi(\gamma, t)$ and $\Gamma(t' = t) = \gamma$, as well as substitute the expression for the injection spectrum normalization, $N = (1/2)n_e(\kappa - 2)(\kappa - 1)\kappa^{-2}\theta^{-3}$ (see Eq. 8), and obtain:

$$N_e(\gamma, t) = \frac{n_e}{2\kappa\theta^2 b_c \gamma^2 t_{\text{growth}}} [\Psi(\gamma) - \Psi(\xi(\gamma, t))] \quad (\text{E.16})$$

One has to consider separately a special case when the $b_c t \geq 1/\gamma$, as this leads to either $\xi \rightarrow \infty$ or $\xi < 0$. Obviously, the latter situation is non-physical, as the Lorentz factor cannot be less than unity. Qualitatively, $b_c t \geq 1/\gamma \rightarrow t \geq 1/(b_c \gamma)$ means that the evolution time of an electron is longer than its cooling time-scale, and in this regime the equilibrium between the injection and cooling is already reached. Therefore, one can easily see that the time-dependent electron spectrum in the Lorentz factor domain $\gamma \geq 1/(b_c t)$ will be ‘‘frozen’’ at the steady-state one. A steady-state solution corresponds to $\xi \rightarrow \infty$, which results in $\Psi(\xi) \rightarrow 0$ (in case $\kappa > 2$). Therefore, the final solution for the time-dependent electron spectrum during the growth phase, is:

$$N_e(\gamma, t) = \frac{n_e}{2\kappa\theta^2 b_c \gamma^2 t_{\text{growth}}} \begin{cases} [\Psi(\gamma) - \Psi(\xi(\gamma, t))], & \text{for } \gamma < (b_c t)^{-1} \\ \Psi(\gamma), & \text{for } \gamma \geq (b_c t)^{-1} \end{cases} \quad (\text{E.17})$$

It is worth to note, that one can obtain the same steady-state solution (the case $\gamma \geq 1/(b_c t)$) by directly solving the kinetic equation (Eq. E.1) with $\frac{\partial N_e}{\partial t} = 0$. To find the electron spectrum at the peak of the flare, i.e. at the moment when the injection is stopped, one simply calculates $N_e(\gamma, t = t_{\text{growth}})$.

Appendix E.2: Deriving time-dependent synchrotron SED during the growth phase

Now let us proceed to the SED and light curve computation. We use the so-called δ -approximation for the electron synchrotron emissivity coefficient. This approximation assumes that a single electron with a Lorentz factor γ emits at a single frequency, rather than a broad spectrum (Rybicki & Lightman 1979):

$$\omega_{\text{peak}} \simeq 0.29\omega_c \quad (\text{E.18})$$

with $\omega_c = 3\gamma^2 eB/(m_e c)$ (averaged over pitch angles), e being the electron charge, and B being the magnetic field (CGS units). From this expression, one obtains:

$$\nu_{\text{peak}} = \frac{\eta e \gamma^2 B}{m_e c} \quad (\text{E.19})$$

where $\eta = (0.29 \times 3)/(2\pi) \approx 0.14$ is a dimensionless numerical factor. For a distribution of electrons, the synchrotron SED in δ -approximation, is given by (Dermer & Schlickeiser 2002):

$$\nu F_{\nu}^{\text{syn}}(\lambda) = \frac{4}{3} \pi R_b^3 \frac{c \sigma_T U_B}{6\pi D^2} \bar{\gamma}^3 N_e(\bar{\gamma}) \quad (\text{E.20})$$

where R_b is the radius of the emitting region, D is the distance between the observer and the source, and $\bar{\gamma}$ is the Lorentz

factor of electrons emitting synchrotron photons with the frequency ν . We obtain this Lorentz factor by expressing it from Eq. E.19:

$$\tilde{\gamma} = \left(\frac{m_e c \nu}{\eta e B} \right)^{1/2} \quad (\text{E.21})$$

Substituting the expression for $N_e(\gamma, t)$ (Eq. E.17), and the expression $b_c = (4\sigma_T U_B)/(3m_e c)$, into the Eq. E.20, we finally obtain the time-dependent SED during the growth phase in δ -approximation:

$$\nu F_\nu^{\text{syn}}(\nu, t) = \frac{n_e R_b^3 \tilde{\gamma} m_e c^2}{12 D^2 t_{\text{growth}} \kappa \theta^2} \begin{cases} [\Psi(\tilde{\gamma}) - \Psi(\xi(\tilde{\gamma}, t))], & \text{for } \nu < \tilde{\nu}(t) \\ \Psi(\tilde{\gamma}), & \text{for } \nu \geq \tilde{\nu}(t) \end{cases} \quad (\text{E.22})$$

where $\tilde{\nu}(t) = (\eta e B)/(m_e c b_c^2 t^2)$ is the frequency corresponding to the condition $\tilde{\gamma} = 1/(b_c t)$.

Appendix E.3: Evaluating the peak light curve flux

To obtain a light curve during the growth phase at a specific frequency of interest ν_* , one has to compute $\nu F_\nu^{\text{syn}}(\nu = \nu_*, t)$. To compute the peak light curve flux, one evaluates the quantity $\nu F_\nu^{\text{syn}}(\nu = \nu_*, t = t_{\text{growth}})$.

Appendix F: Additional Setup for July 22 flare

We also find another setup which reproduce well the July 22 flare data. In such scenario, the magnetic reconnection and so the plasmoid growth phase occurs way before the observing time and the flare is due to the beaming effect combined to the slow decrease of the cooling phase. The peak due to the growth phase occurs during the negative beaming part of the orbit resulting in a low flux comparable to the quiescent state.

Parameter	Symbol	July 22 bis
Plasmoid		
time in EMBLEM at zero observing time [min]	$t_{\text{obs},0}^{\text{emblem}}$	-53
initial orbital radius [GM/c^2]	r_0	15
polar angle [$^\circ$]	θ	135
initial azimuthal angle [$^\circ$]	φ_0	240
initial radial velocity [c]	$v_{r,0}$	0.01
initial azimuthal velocity [c]	$v_{\varphi,0}$	0.5
X position of Sgr A* [μas]	x_0	0
Y position of Sgr A* [μas]	y_0	0
PALN [$^\circ$]	Ω	160

Table F.1. Second orbital parameters of the plasmoid model following a conical motion used for the comparison of the July 22 flares observed by Gravity Collaboration et al. (2018).

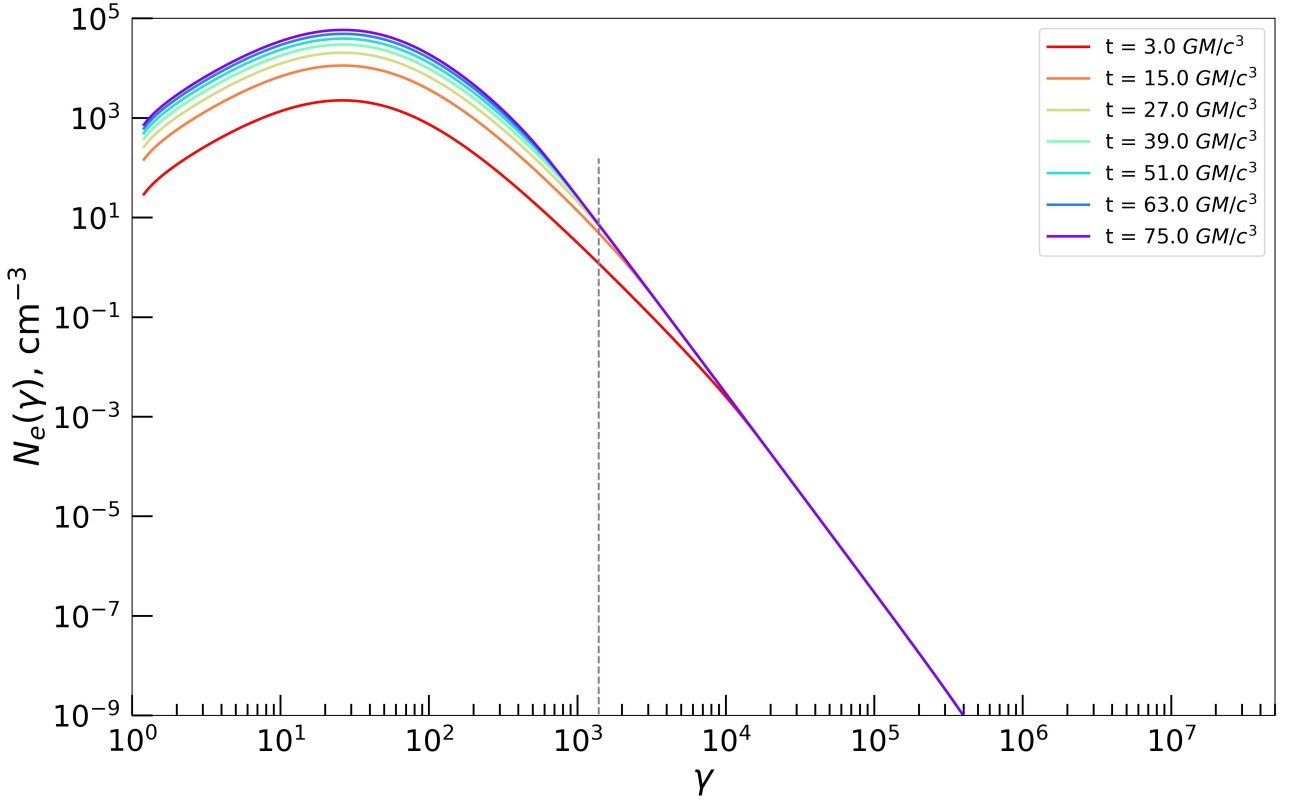


Fig. E.1. Time evolution of the electron distribution with EMBLEM (full lines) from $t = 0$ to $t = t_{\text{growth}} = 75 r_g/c$ injecting a κ -distribution with $\Theta_e = 10$ and $\kappa = 4$ and $n_e = 5 \cdot 10^6 / t_{\text{growth}}$. The magnetic field strength is set to 30 Gauss resulting in a stationary regime for $\gamma > 10^4$ from the very beginning. This regime extends to lower γ values as time grows. For the estimation of the peak flux, we approximate the whole distribution (at $t = t_{\text{growth}}$) by a simple Dirac at $\bar{\gamma}$ represented by the dashed grey line.

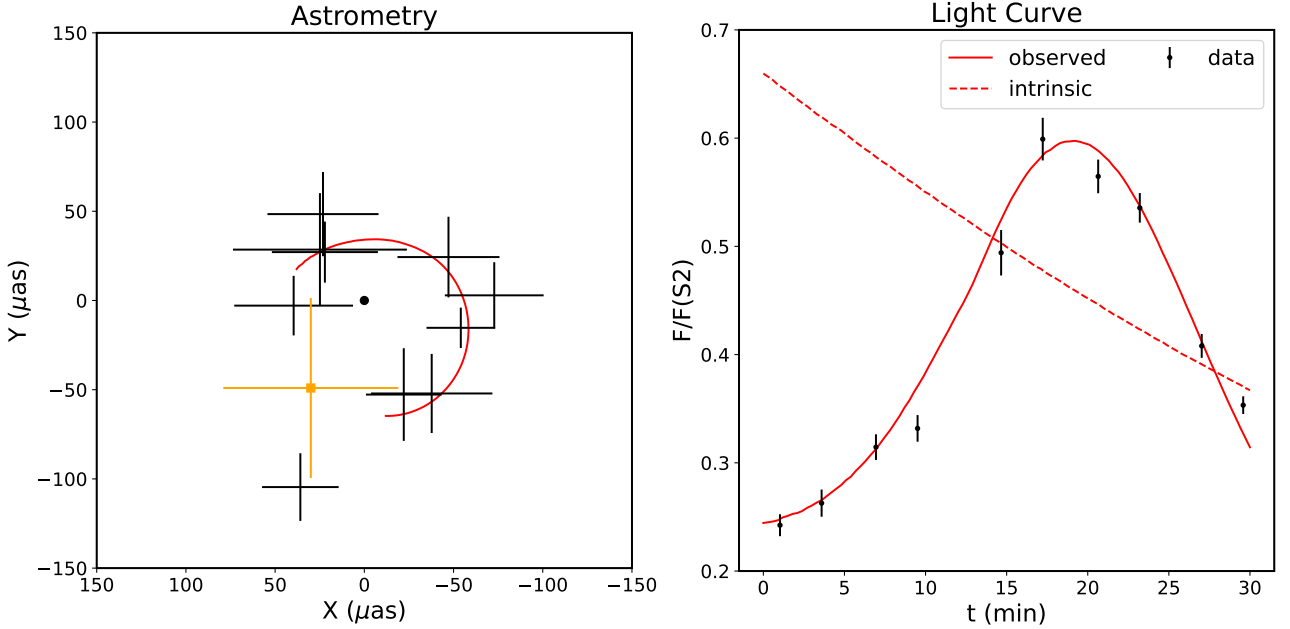


Fig. F.1. Data and plasmoid models of the flares from July 22, 2018. The left panels shows the astrometry of the flare while the right panel shows the light curves. Note that this is not the result of a fit. Contrary to the setup for Fig. 8, the growth time is shorter $t_{\text{growth}} = 50 r_g/c$ resulting into a two peak light curve with the first one occurring at $t = -22$ min but being mitigate by the negative beaming effect. The secondary peak which match the observed flare data shown here is due to the positive beaming during the cooling phase (as shown by the intrinsic light curve). The parameter set for this model is similar to the set of July 22 and is listed in Table F.1 with the same physical parameter as in Table 3 but with $t_{\text{growth}} = 50 r_g/c$, $\Theta_e = 72$ and $B = 10$ G.